AIAA 2001-1027
DSMC Computations for Regions of Shock/Shock and Shock/Boundary Layer Interaction

James N. Moss
NASA Langley Research Center
Hampton, VA 23681-2199
j.n.moss@larc.nasa.gov

39th AIAA Aerospace Sciences Meeting & Exhibit
January 8-11, 2001 Reno, NV

DSMC Computations for Regions of Shock/Shock and Shock/Boundary Layer Interaction

James N. Moss*
j.n.moss@larc.nasa.gov
NASA Langley Research Center, Hampton, VA 23681-2199

This paper presents the results of a numerical study of hypersonic interacting flows at flow conditions that include those for which experiments have been conducted in the Calspan-University of Buffalo Research Center (CUBRC) Large Energy National Shock (LENS) tunnel and the ONERA R5Ch low-density wind tunnel. The computations are made with the direct simulation Monte Carlo (DSMC) method of Bird. The focus is on Mach 9.3 to 11.4 flows about flared axisymmetric configurations, both hollow cylinder flares and double cones. The results presented highlight the sensitivity of the calculations to grid resolution, provide results concerning the conditions for incipient separation, and provide information concerning the flow structure and surface results for the extent of separation, heating, pressure, and skin friction.

Nomenclature

C'	Chapman-Rubesin viscosity constant, $C' = T_\infty \mu^* / T^* \mu_\infty \approx (T_\infty / T^*)^{0.25}$
C_f	friction coefficient, $\tau_w / (0.5 \rho_\infty V_\infty^2)$
C_H	heat transfer coefficient, $q_w / (0.5 \rho_\infty V_\infty^3)$
C_p	pressure coefficient, $(p_w - p_\infty) / (0.5 \rho_\infty V_\infty^2)$
d	maximum double cone diameter, m
F	ratio of simulated to real molecules
k	Boltzmann constant, $1.380658 \times 10^{-23} JK^{-1}$
$Kn_{\infty,L}$	free-stream Knudsen number, λ_∞ / L
L	length from cylinder leading edge to flare, m
L_1	wetted length of first cone
M_∞	free-stream Mach number
n	number density, m^{-3}
p	pressure, N/m^2
q	wall heat transfer rate, kW/m^2
R	reattachment location, m
$Re_{\infty,L}$	Reynolds number, $\rho_\infty V_\infty L / \mu_\infty$
$Re_{\infty,d}$	Reynolds number, $\rho_\infty V_\infty d / \mu_\infty$
s	wetted length, m
S	separation location, m
T	temperature, K
T^*	reference temperature (Eq. 6), K
u	velocity in x-direction, m/s
V_∞	free-stream velocity, m/s
$\overline{\Gamma}$	rarefaction parameter, $\overline{\Gamma} = M_\infty \sqrt{C' / Re_{\infty,L}}$
x,y	model coordinates, m
θ_i	incipient separation angle, deg
λ_∞	mean free path in free stream, m
μ	viscosity, Pa*s
ρ	density, kg/m^3
τ	viscous shear stress, N/m^2
$\overline{\chi}$	hypersonic viscous interaction parameter, $\overline{\chi} = M_\infty^2 \overline{\Gamma}$

Subscripts

w	wall
∞	free stream
ref	reference

Introduction

HYPERSONIC separated flows produce shock/shock and shock/boundary layer interactions that create augmented aerothermal loads and reduced surface control effectiveness, issues critical to hypersonic vehicle design. To enhance the understanding of such flows, experimental and computational studies have been actively promoted by the North Atlantic Treaty Organization (NATO) Research Technology Organization (RTO, formerly AGARD) for basic axisymmetric configurations and for a range of Reynolds numbers. The current study focuses on experimental conditions where separation and reattachment occur under laminar conditions and where the flow is assumed to be steady. Calculations are made by using the direct simulation Monte Carlo (DSMC) method of Bird[1] for both hollow cylinder-flare and double-cone models. The flow conditions simulated include those for which experiments have been conducted in two facilities: the ONERA R5Ch Mach 10 low-density wind tunnel and the Calspan-University of Buffalo Research Center (CUBRC) Large Energy National Shock (LENS) tunnel.

*Senior Research Engineer, Aerothermodynamics Branch, Fellow AIAA.

The hollow cylinder-flare model has a sharp leading edge, a cylinder 101.7 mm long, and a 30° flare. The author has presented extensive calculations (Refs. 2 to 8) for the cylinder-flare model at the ONERA test conditions highlighting the noncontinuum and continuum aspects for the flow, the sensitivity to numerical simulation parameters, the agreement with measurements made in the ONERA wind tunnel, differences in two-dimensional (2D) and axisymmetric results, comparisons with boundary layer (only cylinder or plate results) and Navier-Stokes solutions, and the sensitivity of the calculations for the cylinder portion of the model to numerical parameters. In the present paper, results of new DSMC calculations are included for more energetic flows, as produced in the LENS tunnel for Mach 11 nitrogen flow. These calculations include a parametric range of conditions (free-stream density variations) to identify incipient separation conditions and three test cases for which experiments have been conducted[9] to measure surface heating and pressure distributions.

Calculations for the double-cone models[10] are for flow conditions similar to the hollow cylinder-flare study. For the double-cone configurations investigated, the shock/shock interactions are stronger than those for the hollow cylinder-flare models. The first cone half angle is 25°, while the second cone half angle is 55°. The current double cone configuration produces strong shock interactions because the attached shock from the first cone interacts with the stronger bow shock from the second cone. Also, the outer shocks are modified by the separation and reattachment shocks where the extent of flow separation is significant for the combinations of model size and flow conditions examined. Results are presented that demonstrate the sensitivity of the surface results to numerical parameters, Reynolds number, and flow conditions.

Viscous Interaction and Rarefaction Parameters

In the present study, the characteristic dimension selected for the hollow cylinder-flare is the length from the cylinder leading edge to the flare L, while that selected for the double cone is the maximum diameter d. For the equations in this section, L will be used as the characteristic length. Since moderate to low-Reynolds number results are normally presented as a function of viscous interaction and rarefaction parameters, definitions of those used in the current study are presented.

The free-stream Knudsen number is defined as

$$Kn_{\infty,L} = \lambda_\infty / L \tag{1}$$

where L is the characteristic dimension. Also, the Kn can be expressed in terms of Mach and Reynolds numbers with the following relation

$$Kn_{\infty,L} = 1.276\sqrt{\gamma} M_\infty / Re_{\infty,L} \tag{2}$$

If one uses the boundary layer thickness δ as a characteristic length, then it can be shown that

$$Kn_{\infty,\delta} \sim M_\infty \sqrt{C'/Re_{\infty,L}} \tag{3}$$

which is closely related to the following rarefaction parameter

$$\overline{V} = M_\infty \sqrt{C'/Re_{\infty,L}} \tag{4}$$

where

$$C' = \rho^* \mu^* / \rho_\infty \mu_\infty \approx (T_\infty / T^*)^{0.25} \tag{5}$$

and ρ^* and μ^* are evaluated at a reference temperature given by Ref. 11 (p. 319)

$$\frac{T^*}{T_\infty} = 0.468 + 0.532\,\frac{T_w}{T_\infty} + 0.195\left(\frac{\gamma - 1}{2}\right) M_\infty^2 \tag{6}$$

The 0.25 exponent for the temperature ratio in Eq. 5 results from assuming that the viscosity is a function of the temperature raised to the 0.75 power.

A $\overline{V}$ parameter is often used for correlating pressure and force coefficients. This parameter has also met with some success in correlating heat transfer measurements.[11] The $\overline{V}$ parameter is closely related to the Knudsen number; therefore, the larger the value of $\overline{V}$, the larger the effect of rarefaction.

The hypersonic viscous interaction parameter $\overline{\chi}$ can be expressed is terms of $\overline{V}$ by the following expression

$$\overline{\chi} = M_\infty^2 \overline{V} \tag{7}$$

The induced surface pressure arising from hypersonic viscous interactions is often correlated as a function of $\overline{\chi}$. Large values of $\overline{\chi}$ ($\overline{\chi} > 3$) correspond to strong interaction, while small values of $\overline{\chi}$ ($\overline{\chi} < 3$) denote a weak interaction region. It has been shown[11] that $\overline{\chi}$ is an appropriate viscous correlation parameter for induced pressure changes in both the weak and the strong interaction regions. However, as the flow becomes more rarefied when the leading edge is approached, the continuum assumptions break down, and the measured pressures are considerably less than those predicted by strong interaction theory or those calculated with DSMC.[12] The strong interaction model has a definite upstream limit that appears to be determined by the rarefaction parameter $\overline{V}$ rather than $\overline{\chi}$. The thin Rankine-Hugoniot shock structure breaks down upstream of $\overline{V} \approx 0.15$, where there is a large discrepancy between the measured and Rankine-Hugoniot values of shock density. (Agreement between experimental and DSMC results are shown to be very good in Fig. 12 of Ref. 12). Consequently, $0.15 \le \overline{V} \le 0.20$ is often quoted as the boundary between the strong interaction and merged layer regimes.

As will be demonstrated later, all the experimental test cases considered in the present study are in the strong interaction regime based on the previous expression for $\overline{\chi}$ when evaluated at the location of the deflected surfaces (flare or second cone).

DSMC Code

The DSMC code used in the current study is the general 2D/axisymmetric code of Bird.[1,13] The molecular collisions are simulated with the variable hard sphere (VHS) molecular model. Energy exchange between kinetic and internal modes is controlled by the Larsen-Borgnakke statistical model.[14] For the present study, the simulations are performed by using nonreacting gas models while considering energy exchange between translational, rotational, and vibrational modes. A constant rotational relaxation collision number of 5 was used for the calculations. The vibrational collision number was 50. The reference conditions for the VHS model were as follows: reference temperature = 300 K, temperature exponent of the viscosity coefficient = 0.75, and reference diameters for O_2 and N_2 were 3.96 x 10^{-10} m and 4.07 x 10^{-10} m, respectively. The model surface is assumed to have a specified constant temperature. Full thermal accommodation and diffuse reflection are assumed for the gas-surface interactions.

Common to the DSMC simulations presented is the treatment of the computational domain griding, which consisted of an arbitrary number of regions. Each region is subdivided into cells, and the cells in selected regions are subdivided into subcells to enhance the spatial resolution used to select collision partners. In general, the cell dimensions within a region were nonuniform in both directions, with geometric stretching exceeding an order of magnitude in some regions. Also, the macroscopic quantities are time-averaged results extracted from the individual cells. Since the computational regions were not run with necessarily the same time step, it was essential that steady state conditions be established before generating the final time-averaged results. Steady state was assumed to occur when the total molecules used in the simulation, average molecules in each region, and surface quantities (locations and size of the separation region, and heating) became essentially constant when sampled sequentially over significant time intervals.

Hollow Cylinder-Flare Results

The ONERA hollow cylinder-flare test case considered was formulated initially as one of the test problems concerning shock wave/boundary layer interactions in an AGARD Working Group 18 activity[15] for the validation of Navier-Stokes solvers for cold high-speed flows where the interactions produce large separated regions under laminar conditions. The initial test case generated considerable interest for code validation, as is evident by the AGARD activity[15] and several independent workshops (Ref. 16, for example). Interest in this problem continues with the expansion of test cases to include additional flow conditions and model sizes[17,18] in the current Research Technology Organization (RTO, formally AGARD), working group 10 activities.

A motivation for investigating these test cases with DSMC has been to identify the level of grid resolution and related computational parameters that one must use to achieve accurate results for problems with complex interactions (where the grid resolution is important in directions other than the one normal to the surface). Furthermore, DSMC codes provide a simulation capability that is valid across the entire flow spectrum of free molecular through continuum, a desirable feature for the current problems. However, there are practical limitations when using the DSMC approach due to excessive computational requirements as one moves well into the continuum regime for multiple-dimensional problems.

The current study provides numerical simulations for several sets of hypersonic flow conditions (Table 1), where some of the conditions are those for which tests have been conducted in the ONERA R5Ch low density wind tunnel and the CUBRC LENS tunnel. The LENS test conditions denoted as LENS-19, LENS-11, and LENS-9 are conditions for which tests have been completed by CUBRC. Results of the CUBRC tests are not currently available for comparison with calculations; however, experimental measurements for surface heating and pressure distributions will be made available in Ref. 9. The remaining LENS conditions have an alphabetic letter extension which denote either a pretest nominal condition (LENS-A) or an assumed condition resulting from parametric variations of the free-stream density for the LENS-9 condition producing the LENS-B through LENS-G conditions. The order of magnitude variation in density provides a range of conditions that allows one to identify the conditions that produce incipient separation for the current axisymmetric configuration and the nature of the viscous and shock/shock interactions for free-stream Reynolds numbers in the range of 2 500 to 25 000.

Details of the model configuration used in the ONERA tests are presented in Fig. 1. The hollow cylinder has a sharp leading edge with a bevel angle of 15° and is aligned parallel to the oncoming flow. The compression flare is inclined 30° to the cylinder and is terminated by a hollow cylindrical section. Additional information concerning model construction, materials, and instrumentation is given in Refs. 6 and 19.

For the CUBRC tests, two hollow cylinder-flare configurations are used as described in Refs. 17 and 18 one that mimics the ONERA model and will be referred to as the "short" flare (current calculations use the dimensions shown in Fig. 1 for describing the

model outer surface for both the ONERA and the LENS short-flare model) and a model with a much longer flare. For the long-flare model, the horizontal length of the flare (referred to as the long flare) is 118.28 mm rather than the 43.3 mm shown in Fig. 1, and the model terminates at the end of the flare no cylindrical extension.

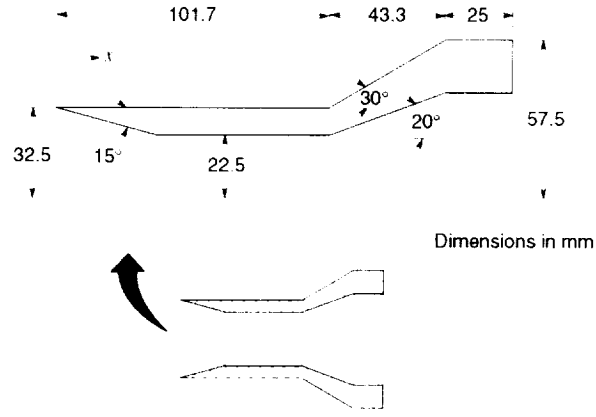

Fig. 1 ONERA hollow cylinder-flare model (x measured from leading edge and L = 101.7 mm).

Calculations for R5Ch Conditions and Comparison with Measurements

Figures 2 through 8 present results of the calculations first reported in Refs. 4 and 5 that describe the flow-field features and surface results for the ONERA hollow cylinder-flare test case. The experimental value for free-stream Reynolds number is 18916, where the viscosity (3.29×10^{-6} Pa * s) is given by the Sutherland expression and the characteristic dimension is the cylinder length L. Also presented are comparisons of the surface results for heating, pressure, and the extent of separation with the experimental measurements described in Refs. 6, 7, and 19. The current results are those obtained with the finest grid resulting from the grid resolution study described in Ref. 4. The previous calculations show that the extent of separation is quite sensitive to the grid a much smaller separation region is obtained with a coarse grid. Data included in Fig. 2 provide information concerning the grid and simulation parameters for the finest grid solution. A four-region computational domain was used where each cell was subdivided into four subcells (2 x 2). The time step in each of the four regions had values of 75, 75, 28, and 15 ns, respectively.

General flow features for this test case are evident in Figs. 2 and 3. Figure 2 shows selected Mach contours and streamlines, while Fig. 3 presents the normalized density contours. Evident is a large separation region characterized by a single vortex embedded in the subsonic flow region. Calculated locations for separation and reattachment (denoted by S and R, respectively) are 76.76 mm and 134.4 mm downstream of the cylinder leading edge. The shock/shock interaction occurs near the end of the flare where the shock layer thickness is at a minimum and the density is at a maximum, equal to 14.4 times the free-stream value.

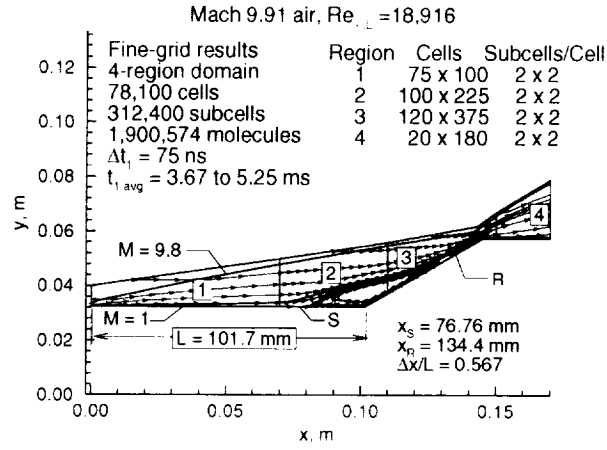

Fig. 2 Flow structure and simulation parameters for ONERA hollow cylinder flare at R5Ch conditions.

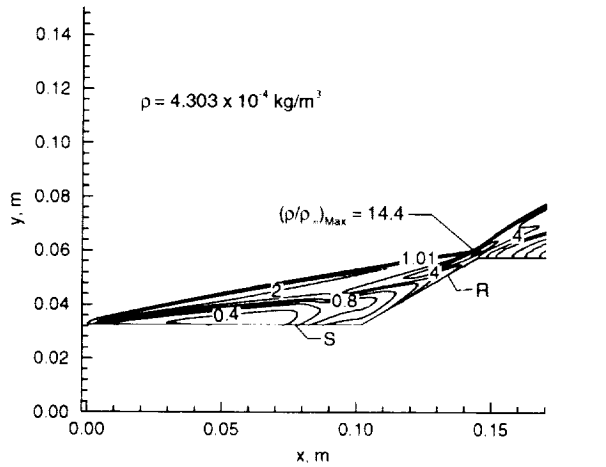

Fig. 3 Density contours for ONERA hollow cylinder flare at R5Ch conditions.

Figures 4 through 6 present the calculated surface results for skin friction coefficient, heating rate, and pressure coefficient as a function of the distance from the cylinder leading edge (normalized by the cylinder length L). Maximum values for friction, heating rate, and pressure occur on the flare at a location downstream of reattachment very close to the end of the flare located at x/L = 1.426. Included in these figures are the results of the experimental measurements[6,7] for the extent of separation as inferred from oil flow measurements, heating rates extracted by using a thin-film technique, and surface pressure inferred from variable reluctance differential transducers connected to the model pressure taps by tubes.

Agreement between the calculated and the measured

Table 1 Free-stream and surface conditions for hollow cylinder-flare calculations.

Condition	V_∞, m/s	n_∞, m^{-3}	T_∞, K	ρ_∞, kg/m^3	p_∞, N/m^2	M_∞	$Re_{\infty,L}$	Gas	T_w, K
R5Ch	1418.7	8.950×10^{21}	51.0	4.303×10^{-4}	6.3	9.91	18916	Air	293.0
LENS-A	2718.6	1.463×10^{22}	194.1	6.808×10^{-4}	39.2	9.57	14920	N_2	297.8
LENS-19	2575.6	1.850×10^{22}	121.7	8.607×10^{-4}	31.1	11.45	25360	N_2	296.1
LENS-11	2609.1	1.089×10^{22}	128.9	5.066×10^{-4}	19.4	11.28	14490	N_2	297.2
LENS-9	2566.4	1.817×10^{22}	121.1	8.452×10^{-4}	30.4	11.44	24910	N_2	296.7
LENS-B	2566.4	1.240×10^{22}	121.1	5.770×10^{-4}	20.7	11.44	17000	N_2	296.7
LENS-C	2566.4	1.021×10^{22}	121.1	4.751×10^{-4}	17.1	11.44	14000	N_2	296.7
LENS-D	2566.4	8.022×10^{21}	121.1	3.732×10^{-4}	13.4	11.44	11000	N_2	296.7
LENS-E	2566.4	7.293×10^{21}	121.1	3.393×10^{-4}	12.2	11.44	10000	N_2	296.7
LENS-F	2566.4	5.105×10^{21}	121.1	2.375×10^{-4}	8.5	11.44	7000	N_2	296.7
LENS-G	2566.4	1.817×10^{21}	121.1	8.452×10^{-5}	3.0	11.44	2491	N_2	296.7

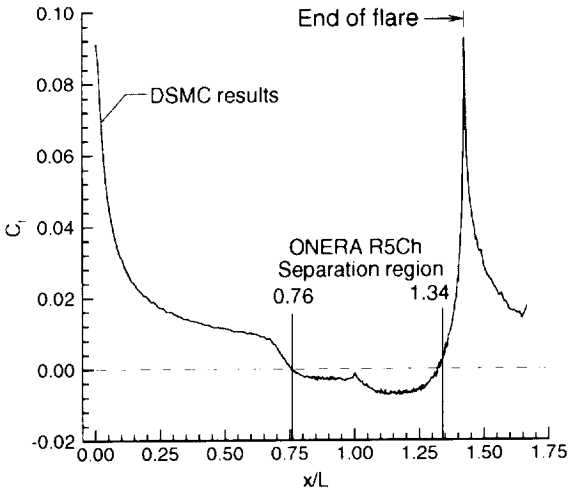

Fig. 4 Skin friction coefficient and extent of separation (oil-flow data from experiments).

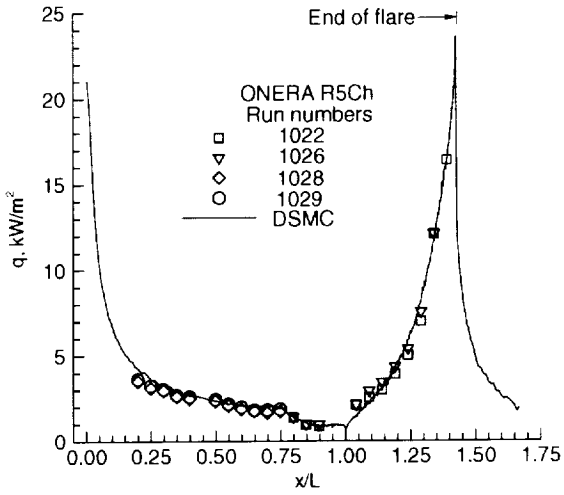

Fig. 5 Heat-transfer rate distributions.

results are very good for the extent of separation and the heating rate distribution; however, there are noticeable differences for the pressure distribution. The separation location is the same for both sets of results. The calculated reattachment location occurs, however, somewhat forward of the experimental value, and the extent of the calculated separation ($\Delta x/L$) is 98% of the measurement. The heating-rate distributions are characteristic of those for laminar flows in that the heating shows an initial decrease at the location of separation ($x/L = 0.76$), a cusp-like behavior at the juncture, and a rapid increase along the flare.

Among the surface quantities, the agreement between the current calculations and measurements is the poorest for pressure. This discrepancy is particularly puzzling since the agreement for both heat transfer and the locations for separation and reattachment are very good. The trends of the two data sets are qualitatively consistent; however, the computational results are consistently higher than the measured values. As first pointed out in Ref. 4, the 42% discrepancy near the peak pressure location on the flare is very obvious; however, differences of this magnitude are also present along the hollow cylinder. In fact, this difference is a constant. If the experimental pressure values are multiplied by a factor of 1.4, agreement between the two data sets becomes very good, as shown in Figs. 7 and 8, where Fig. 8 presents an enlarged view focusing primarily on the cylinder.

Additional results are presented in Ref. 8 that address the lack of agreement along the cylinder between calculation and measurement where the sensitivity of the surface and flow-field results to variations in the numerical parameters used in the results were discussed earlier; in particular, to determine if the calculated surface pressure is influenced by additional refinements and leading edge treatments. Surface results for pressure (see Ref. 8 for heating rate and flow-field profile sensitivity) are given in Fig. 9. The influence of the flare on the hollow cylinder-flare (denoted as H.C.F in Fig. 9) results extends slightly upstream of

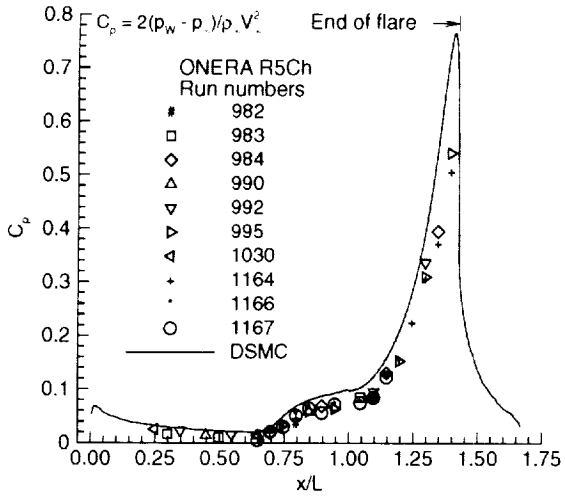

Fig. 6 Pressure coefficient distributions.

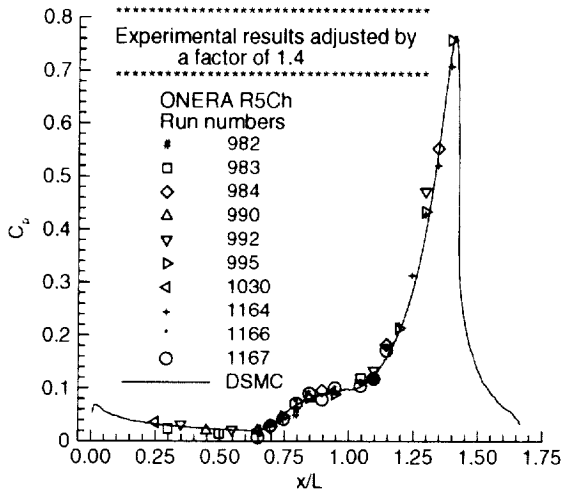

Fig. 7 Pressure coefficients—experimental data adjusted.

the x = 70 mm location, clearly evident in the surface pressure distribution. Also, the outflow boundary condition imposed (free stream at the end of the cylinder) has an influence on the surface pressure results that extends about 6 mm upstream of the cylinder termination. The parametric variations for each of the five cylinder calculations are as follows: Case 1 was a one-region computational domain identical to that used in the H.S.F. simulation (see Fig. 2); for Case 2, the number of cells and subcells were increased by a factor of three (140 x 150 cells), and the time step was 20% of that for Case 1 (15 ns); Case 3 used a time step of 25 ns and the same cell resolution as H.C.F. and Case 1; Case 4 used a time step of 25 ns and the same grid resolution as the H.C.F. but had two extra regions, with additional treatment in front of and downstream of the leading edge (a region upstream of

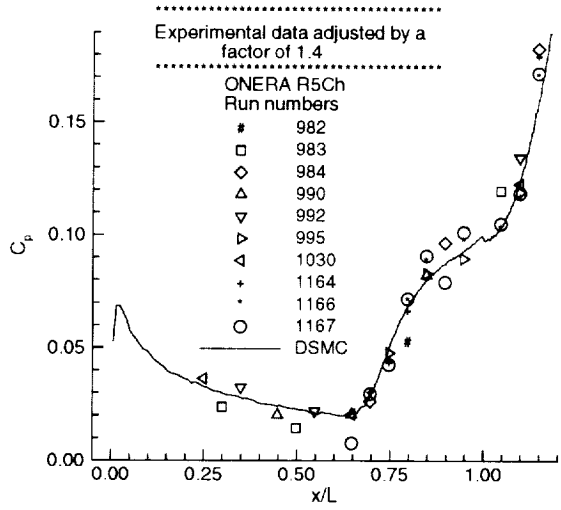

Fig. 8 Cylinder pressure coefficient distributions—experimental data adjusted.

the leading edge [-3 mm] and a region that extended a short distance [3 mm] downstream of the leading edge with five times the Δx resolution of the H.S.F case). Case 5 differed from Case 4 in that it included two additional regions to account for the influence of the beveled leading edge underside. Common to all the solutions were the four subcells/cell and a scaling of real-to-simulated molecules such that there were, on average, approximately 25 simulated molecules per cell. When the surface results for pressure and heating rate (not shown, see Ref. 8) distributions are compared with the H.S.F. results, there is no effect other than the expected results very near the leading edge as the cell dimension in the x-direction (Δx) decreases near the leading edge, one gets an improved definition of the surface quantities where a local maximum occurs and then decreases in value as the leading edge is approached (quantities are decreasing toward their free molecular values but will not achieve the free molecular values because of upstream influence). As for the impact of these additional refinements on the downstream flow-field quantities, no impact is evident on the density profiles at x/L locations of 0.3 and 0.6, as shown in Ref. 8. The conclusion[8] was that the DSMC results presented earlier for surface pressure are correct for the cylinder and should be reasonably accurate for the flare, based on a constant discrepancy of 40% with measurements for both cylinder and flare. Also, the current DSMC results are in good agreement with those obtained by Markelov et al.[21] for the ONERA test case, in which a different DSMC code was used.

Flow-field density measurements have also been performed at ONERA for the hollow cylinder-flare model by detecting X-ray emissions from the gas produced by electron beam impact. The experimental results have been compared[7] with numerical results obtained

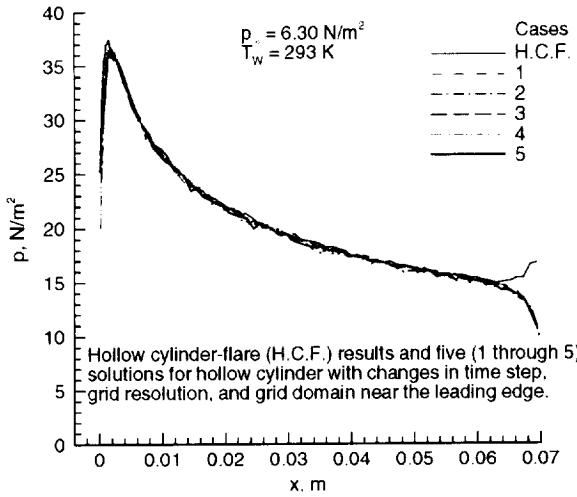

Fig. 9 Effect of simulation parameters on cylinder pressure distributions R5Ch conditions.

by using the current DSMC results and two Navier Stokes codes. The agreement between measurements and calculations is somewhat mixed because neither DSMC nor Navier Stokes results provided consistent agreement with the measurements made at three locations (x/L = 0.3, 0.6, and 0.76) along the cylinder. Details concerning these measurements and comparisons are given in Ref. 7.

Calculations for LENS and LENS-Like Conditions

Four subsections are used to present the calculations made for LENS or LENS-like flow conditions. The first section describes the calculations made for a set of nominal pretest conditions denoted as LENS-A, where the sensitivity of surface results and the extent of separation are demonstrated for grid (cell/subcell) resolution and length of flare (short versus long flare). Insight and experience gained from this portion of the study were then used to perform the computations for three CUBRC experimental test cases (LENS-19, -11, and -9). Results for surface and flow-field structure are presented in the second subsection for each of the three test cases. The third subsection presents the results of calculations used to identify the conditions for incipient separation by arbitrarily varying the free-stream density of the LENS-9 test condition. The fourth subsection discusses the results of the current calculations when presented in the form of conventional correlations.

Tabulated results from the calculations concerning the extent of separation and the sensitivity of the results to various cell/subcell combinations are included in Table 2, while information concerning maximum pressure and heating-rate values along the 30° flare are presented in Table 3.

Results for LENS-A conditions pretest conditions

This section presents results of DSMC calculations for flow about both the short- and long-flare hollow cylinder-flare models at a nominal LENS flow condition (Table 1), where the flow is Mach 9.57 nitrogen at a free-stream Reynolds number of 14920 (characteristic length is the cylinder length, L = 101.7 mm, and the viscosity is given by the VHS[1] model). The flow is more energetic than the R5Ch conditions; however, the flow enthalpy is still quite low, and chemical reactions are neglected for this test case condition. As previously discussed, the short flare model was assumed to have the same outer surface dimensions as the ONERA model (Fig. 1), while the long-flare model has simply an extended flare with the model terminated at the end of the flare. The long-flare model was included[17] in the experimental program to allow for a complete pressure recovery on the flare, thus making a more straightforward comparison with theoretical models. The current results provide an indication of the sensitivity of the DSMC calculations to grid resolution, show that the extent of separation is much smaller than that for the R5Ch flow conditions, show that the results for the long and short flare are essentially identical within the domains common to the two models, and provide information concerning the general features of the surface results and flow-field structure.

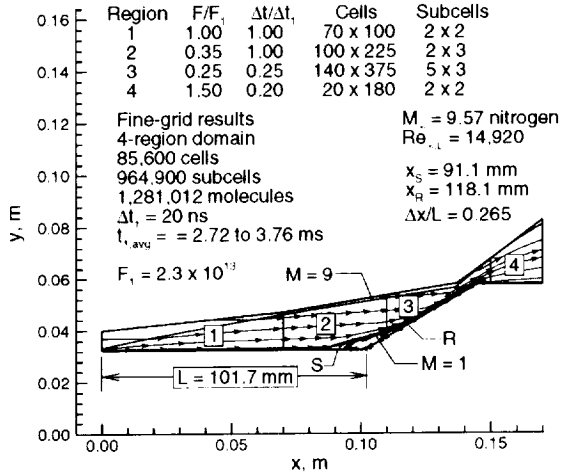

Fig. 10 Flow structure and solution parameters for LENS-A condition with short flare.

Figures 10 and 11 provide information describing the computational domain, simulation parameters, flow structure (selected Mach contours and streamlines), and calculated locations for separation and reattachment for the short and long flare CUBRC models, respectively. (The symbol F in Figs. 10 and 11 denotes the ratio of real to simulated molecules.) These results are for the finest grid calculations resulting from several computations where grid refinement and

Table 2 Grid information, flow parameters, and separation results for hollow cylinder-flare calculations.

Condition	Flare	Cells	Subcells	M_∞	$Re_{\infty,L}$	$Kn_{\infty,L}$	$\overline{V}$	$\overline{\gamma}$	x_S, mm	x_R, mm	$\Delta x/L$
LENS-A	Short	85 600	964 900	9.57	14 920	0.00077	0.064	5.86	91.11	118.12	0.265
LENS-A	Short	85 600	531 200	9.57	14 920	0.00077	0.064	5.86	90.70	118.60	0.274
LENS-A	Long	142 000	1 344 250	9.57	14 920	0.00077	0.064	5.86	91.13	117.87	0.263
LENS-A	Long	49 625	147 500	9.57	14 920	0.00077	0.064	5.86	93.56	116.09	0.222
LENS-A	Long	49 625	49 625	9.57	14 920	0.00077	0.064	5.86	94.79	115.04	0.199
LENS-19	Short	88 100	979 900	11.45	25 360	0.00055	0.057	7.42	78.45	125.68	0.464
LENS-19	Short	85 600	85 600	11.45	25 360	0.00055	0.057	7.42	77.61	125.68	0.473
LENS-11	Long	142 000	1 344 250	11.28	14 490	0.00094	0.074	9.44	99.59	106.35	0.066
LENS-9	Long	146 250	1 366 250	11.44	24 910	0.00055	0.057	7.40	79.72	125.07	0.446
LENS-9	Long	142 000	142 000	11.44	24 910	0.00055	0.057	7.40	77.18	126.00	0.480
LENS-B	Short	85 600	954 100	11.44	17 000	0.00081	0.069	9.05	94.94	117.84	0.225
LENS-C	Short	85 600	954 100	11.44	14 000	0.00099	0.076	9.98	100.86	104.02	0.031
LENS-D	Short	85 600	954 100	11.44	11 000	0.00126	0.086	11.21	101.67	102.02	0.003
LENS-E	Short	85 600	954 100	11.44	10 000	0.00138	0.090	11.72	-	-	0.000
LENS-F	Short	85 600	436 600	11.44	7 000	0.00197	0.108	14.09	-	-	0.000
LENS-F	Short	85 600	85 600	11.44	7 000	0.00197	0.108	14.09	-	-	0.000
LENS-G	Short	60 000	60 000	11.44	2 491	0.00554	0.180	23.55	-	-	0.000
LENS-G	Long	96 780	96 780	11.44	2 491	0.00554	0.180	23.55	-	-	0.000

Table 3 Maximum pressure and heating rate values along 30° flare.

Condition	Flare	x_{ref}, mm	p_{ref}, N/m^2	q_{ref}, kW/m^2	p_{max}/p_{ref}	q_{max}/q_{ref}
LENS-A	Long	84.15	66.66	22.16	33.08	15.05
LENS-A	Short	84.15	65.15	21.52	34.15	15.61
LENS-19	Short	70.21	63.38	19.53	53.27	21.29
LENS-11	Short	92.61	41.38	14.63	39.14	16.14
LENS-9	Long	71.06	60.44	18.93	53.08	20.97
LENS-B	Short	83.74	42.89	14.92	42.78	17.31
LENS-C	Short	90.92	36.62	13.65	40.69	15.70
LENS-D	Short	90.50	30.23	12.31	39.30	14.84
LENS-E	Short	90.08	28.04	11.95	38.85	14.30
LENS-F	Short	90.05	21.62	10.43	35.87	13.06
LENS-G	Long	87.96	9.40	7.12	26.79	9.44

sensitivity studies were performed. Figure 12 is an example of the results for the long-flare model, showing the sensitivity of heating rate to different combinations of regions, cells, and subcells a factor of 27 in subcell resolution. The effect of grid resolution on heating shows the expected trend of decreased heating with improved grid resolution outside the surface areas influenced by flow separation. Also, the size of the separation zone increases with improved grid resolution, as indicated by the tabulated results for $\Delta x/L$ included in Fig. 12. The peak heating downstream of reattachment is slightly higher for the finer grid results.

The results presented in Fig. 12 do not demonstrate grid convergence; however, results for the short flare model, where the grid was identical to that for the long flare model for regions 1 through 3, showed that the surface results were in close agreement for two solutions, where one solution had the cell/subcell arrangement given in Fig. 10 (same as for the long flare solution for regions 1 through 3) and the one with the same number of cells (85 600) but only about half the number of subcells (531 200).

Comparisons of surface results for the short and long flare models are presented for heating coefficient, pressure coefficient, and skin friction coefficient in Figs. 13, 14, and 15, respectively. The results show that the surface quantities are essentially identical for surfaces common to the short and long flare models. For this particular LENS nominal test condition, the extent of separation is only 47% of that calculated and measured for the ONERA R5Ch test condition.

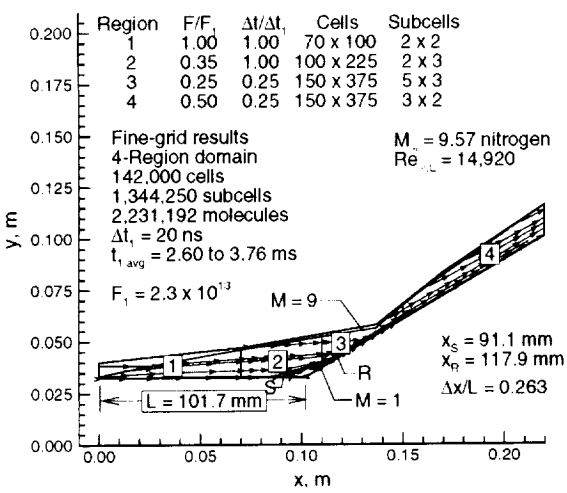

Fig. 11 Flow structure and solution parameters for LENS-A condition long flare.

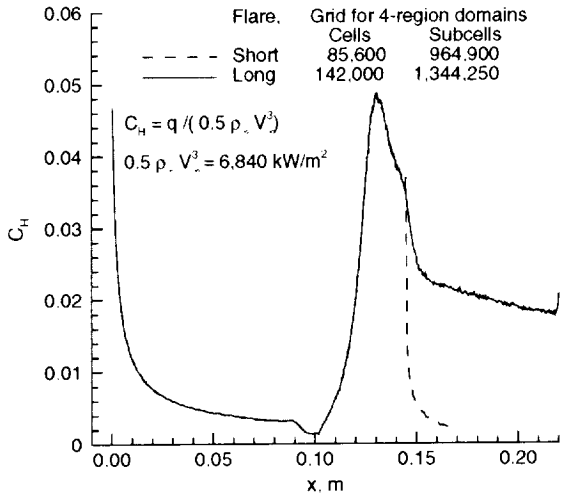

Fig. 13 Heat-transfer coefficient results for LENS-A condition.

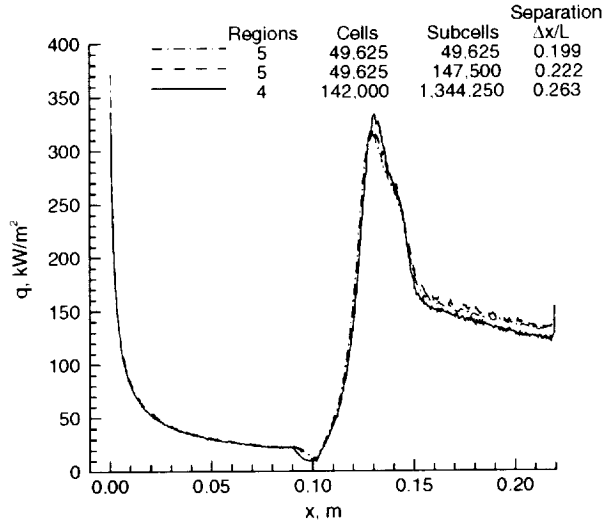

Fig. 12 Effect of grid on heating rate—long flare at LENS-A condition.

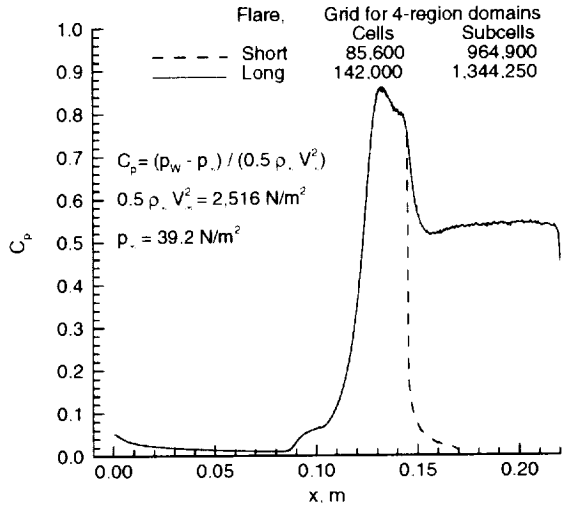

Fig. 14 Pressure coefficient results for LENS-A flow condition.

With the smaller extent of separation, the calculations suggest that the short flare is sufficiently long to negate any influence of the expansion at the end of the flare on the reattachment location. However, the end of flare expansion produces a thinning of the boundary layer and significant changes in the surface quantities decreasing pressure (Fig. 14) and increasing heating (Fig. 13) and friction (Fig. 15). The same trends are evident for the short-flare model where the flow expands to the cylindrical extension at x = 0.145, as is clearly evident in the heating and friction results (also examine Fig. 16).

Composite plots for heating rate, pressure, and skin friction are given in Figs. 16 and 17 for the short- and long-flare models, respectively. These data sets provide information on the correlation of the three surface quantities and explain how they are influenced by separation. The general qualitative features are the same as previously discussed for the R5Ch test conditions.

Figures 18 through 20 provide information describing the flow structure for the short flare. Contours for nondimensional density, overall kinetic temperature, and scalar pressure (nkT, where T is the overall kinetic temperature) are included. The flare-induced adverse pressure gradient is evident in Fig. 20 where the isopressure lines coalesce into a separation shock that compresses the flow to a maximum density of 29.6 times the free-stream value. Along the surface and downstream of reattachment are the locations for maximum density and scalar pressure, with magnitudes equal to 29.6 and 57.2 times their respective free-stream values. When the current calculated re-

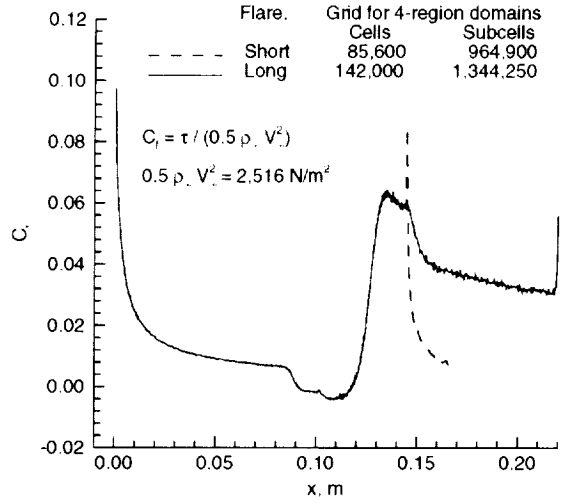

Fig. 15 Skin friction coefficient results for LENS-A flow condition.

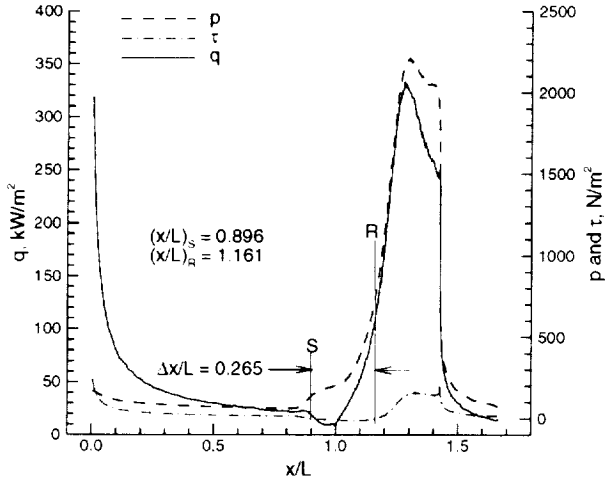

Fig. 16 DSMC surface results for LENS-A condition (short flare).

sults for the LENS-A condition are compared with the calculated results for the R5Ch flow conditions, the maximum density is 3.25 times greater and occurs at the surface rather than in the shock layer as it does for the R5Ch case (Fig. 3). Also, the temperatures are much higher, the maximum temperature being 2.8 times greater. For the maximum scalar pressure, the calculated LENS value is 6.2 times that calculated for the R5Ch condition. Additional details concerning the calculations for the LENS-A condition, particularly body normal profiles, are included in Ref. 8.

The experience resulting from the calculations of the LENS-A condition influenced the approach that was used for simulating three LENS test conditions discussed in the next section.

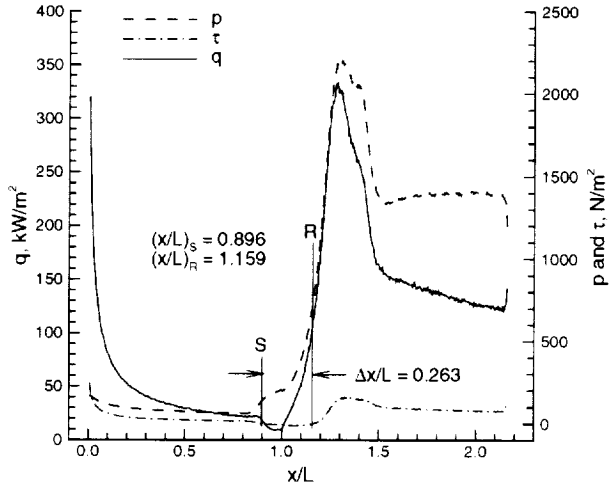

Fig. 17 DSMC surface results for LENS-A condition (long flare).

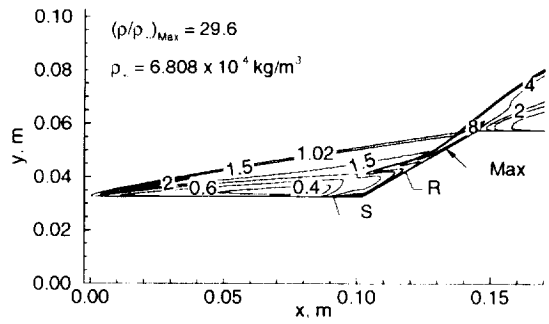

Fig. 18 Density contours for LENS-A condition (short flare).

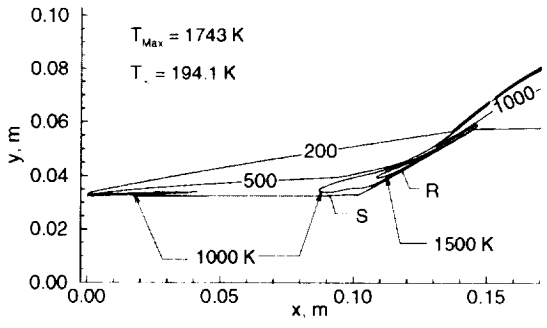

Fig. 19 Overall kinetic temperature contours for LENS-A condition (short flare).

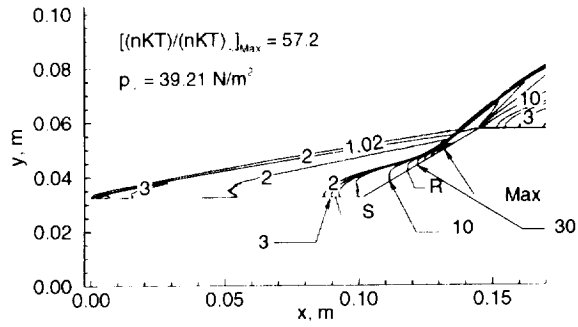

Fig. 20 Scalar pressure contours for LENS-A condition (short flare).

Calculations for LENS test cases 11, 19, and 9

This section presents the results of DSMC calculations for three experiments conducted at CUBRC[9] with the LENS tunnel. The three test conditions (Table 1) are denoted as LENS-11, LENS-19, and LENS-9. Based on the $\overline{\chi}$ and $\overline{V}$ parameters as previously defined, the flow for each of these test conditions is in the merged layer regime ($\overline{V} > 0.15$) for at least the first 10% of the cylinder length, while the remaining flow along the cylinder is in the strong interaction regime ($\overline{\chi} > 3$).

Even though many figures are presented describing the results (Figs. 21 through 58), the discussion will be brief since the material presented is repeated for each of the three test cases, and the format for presentation is similar to that used previously for presenting the LENS-A results. The experimental measurements for surface heating and pressure will be presented for the first time in Ref. 9. The three test conditions are for Mach 11 nitrogen and Reynolds numbers of 14000 and 25000. The LENS-11 condition is for a higher Mach number than the pretest LENS-A condition, but for approximately the same Reynolds number condition. Consequently, the LENS-11 viscous interaction and rarefaction parameters are greater than the corresponding values for LENS-A (Table 2). Therefore, no grid sensitivity study was made for this test condition (more rarefied); instead, a grid similar to that used for the finest grid LENS-A calculation was used. As expected, results for the current calculations show that the flow structure for LENS-11 is different from that for the LENS-A condition in that a much smaller separation region is calculated (a $\Delta x/L$ equal 0.066 rather than 0.263), indicative of the very strong effect of Mach number for interacting hypersonic flows.

The observed effect of Mach number is consistent with the experimental findings of Holden[22] and Delery[23] which show that the upstream influence and separation length decrease with Mach number for fixed ramp angle and Reynolds number. The LENS-11 and LENS-A computations are for the same flare angle, essentially the same Reynolds number, and Mach numbers of 11.28 and 9.57, respectively. The normalized extent of separation and upstream influence (distance from cylinder-flare junction to the upstream separation location) for the two flow conditions are 0.066/0.021 and 0.263/0.104, respectively.

The LENS-19 and LENS-9 cases are for higher Reynolds number conditions than LENS-11 and the flow conditions are approximately the same for these two test cases. The only significant difference for the two flow cases is with the test model configuration — short flare for LENS-19 and long flare for LENS-9. Since these two test cases were at higher Reynolds number conditions, two solutions were generated for each test case. The first solution was made without subcells, while the second solution was made with approximately the same cell arrangement (minor tuning) and time steps, but with a significant number of subcells, particularly in the regions where separation and reattachment occurred — regions 2 and 3, respectively. The additional spatial resolution provided by the subcells, for the current cell resolution, has a small impact on the extent of separation (Table 2) and surface results (Figs. 57 and 58); in fact, the extent of separation is slightly smaller with subcells, as was the case for the LENS-A short flare calculations. The subsequent results will show that the calculated flow-field and surface quantities for LENS-19 and LENS-9 cases are essentially the same. Also, the calculated effect of short versus long flare (LENS-9 versus LENS-19) has no obvious impact on the flow structure or extent of separation (Table 2), as were the results for the LENS-A condition.

Figures 21 through 53 present information for each of the three experimental test cases with respect to the following quantities: numerical simulation parameters; information concerning simulation history; calculated surface heating, pressure, and skin friction distributions; flow-field contours for density, overall kinetic temperature, scalar pressure; and radial profiles for density, pressure, temperature, and tangential velocity at various locations along the cylindrical portion of the model. These results are for the finest grid solutions (Table 2).

The only additional information presented in this section that was not discussed for the LENS-A calculations is the simulation history data, Figs. 22, 33, and 44. These results provide a history of the simulation in terms of the total number of molecules and the average number of molecules per cell for each computational region. As noted previously, the current calculations are not time accurate in that the flow regions are not advanced with the same time step. Details on a regional basis are useful in identifying necessary, but not necessarily sufficient conditions that should be satisfied before time-averaged results are extracted. The current results indicate that the time to achieve a steady state condition increases substantially as the extent of separation increases. This

behavior is demonstrated for LENS-11 and -19 (see Figs. 22 and 33) where the calculated extent of separation ($\Delta x/L$) is 0.066 and 0.464, respectively, and the time required to approach a quasi-steady or steady state is much longer for the LENS-19 case.

For the two higher Reynolds number conditions, nonequilibrium aspects of the flow are clearly evident (for example, Figs. 39 through 42 for the LENS-19 results) along the cylindrical portion of the model where temperature jump and velocity slip are present. A lack of translational equilibrium occurs because the individual translational temperature components (not shown) differ substantially, particularly adjacent to the surface. Consequently, the scalar pressure (nkT) of the gas adjacent to the surface is not the same as the surface normal pressure (p_w, the normal force per unit area exerted by the gas on the surface). The scalar pressure adjacent to the surface is greater than the surface normal pressure. Additionally, the surface normal scalar pressure profiles experience substantial gradients adjacent to the surface along much of the cylinder (Figs. 40 and 51).

Figures 54 through 56 provide a comparison of the calculated heating, pressure, and friction coefficients for the three LENS test conditions. The LENS-19 and LENS-9 conditions produce essentially the same surface results for the two test configurations short and long flare, respectively. Also, the pressure overexpansion and recompression along the flare is more significant for the higher Reynolds number cases, and this pressure response is clearly evident in the heating (Fig. 54) and friction (Fig. 56) results.

The effect of additional grid refinement by means of increasing the number of subcells produces very small changes in the extent of separation for the LENS-19 and -9 cases. For the calculated surface distributions, again, the additional grid refinement had negligible impact on the results, as is demonstrated by the heat transfer and pressure coefficient comparisons for the LENS-19 results shown in Figs. 57 and 58, respectively. Of course, if the cell resolution had been much coarser initially, then there would have been a very clear impact of additional grid refinement by either increasing the number of cells or subcell, as is somewhat evident in the results of Fig. 12.

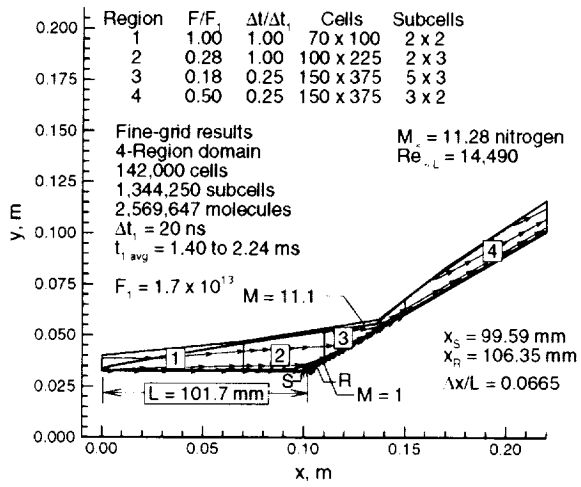

Fig. 21 Flow structure and solution parameters for LENS-11 condition.

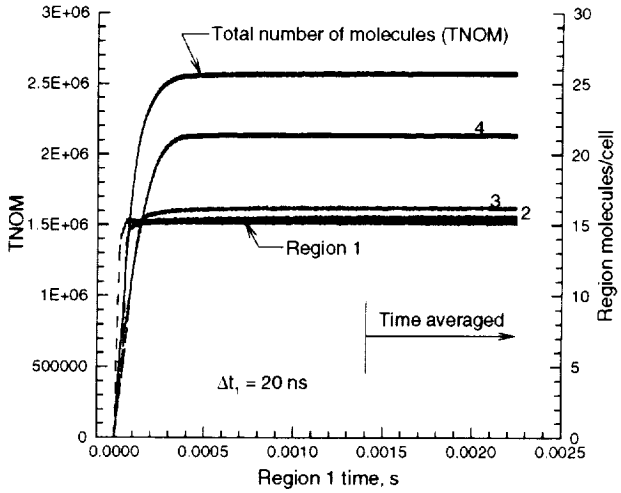

Fig. 22 Simulation history for LENS-11 condition.

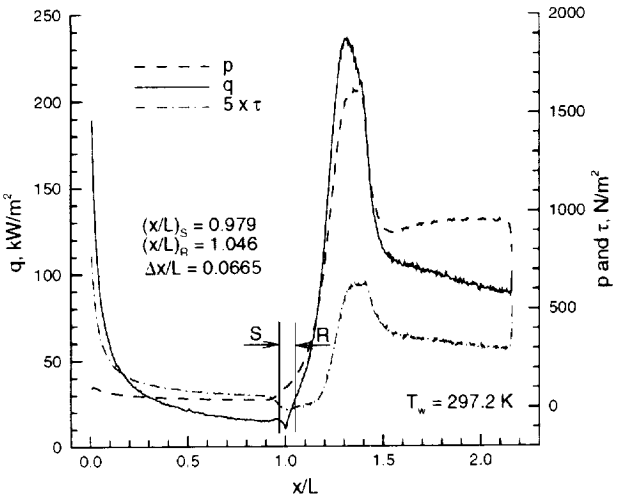

Fig. 23 Surface distributions for LENS-11 condition.

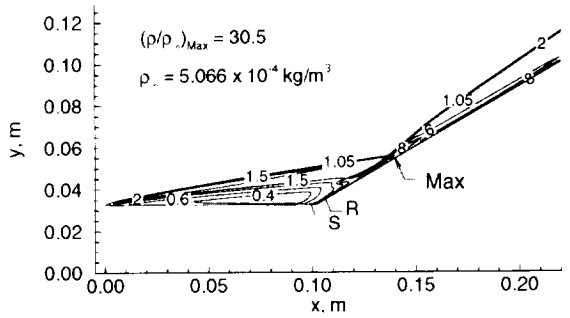

Fig. 24 Density contours for LENS-11 condition.

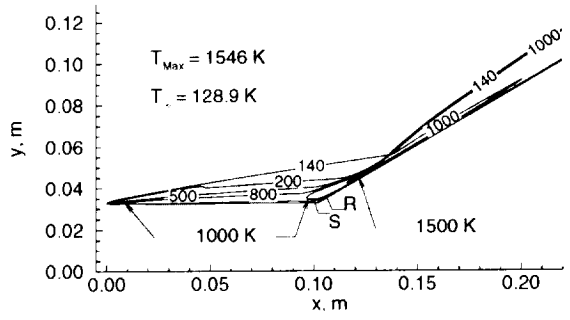

Fig. 25 Overall kinetic temperature contours for LENS-11 condition.

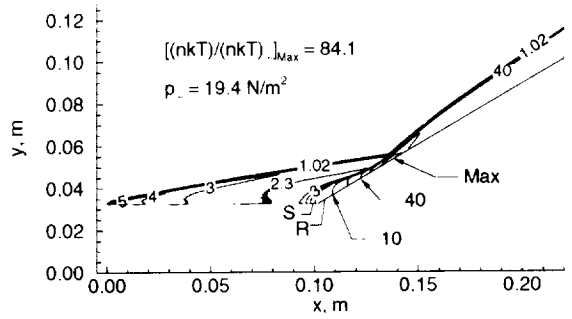

Fig. 26 Scalar pressure contours for LENS-11 condition.

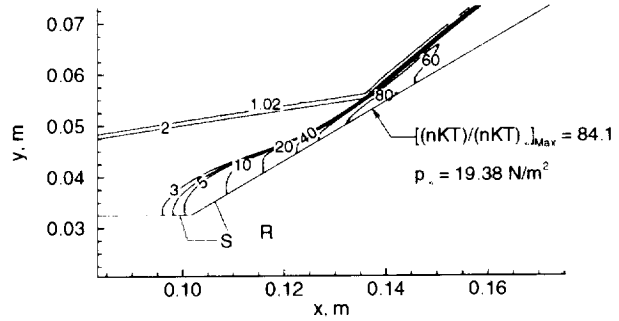

Fig. 27 Scalar pressure contours along flare for LENS-11 condition.

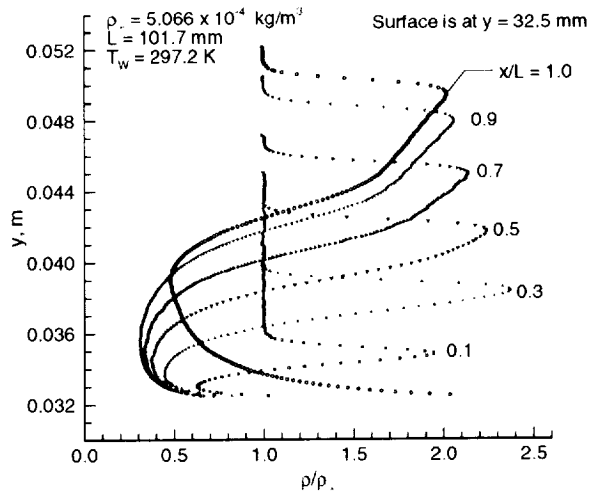

Fig. 28 Density profiles for LENS-11 condition.

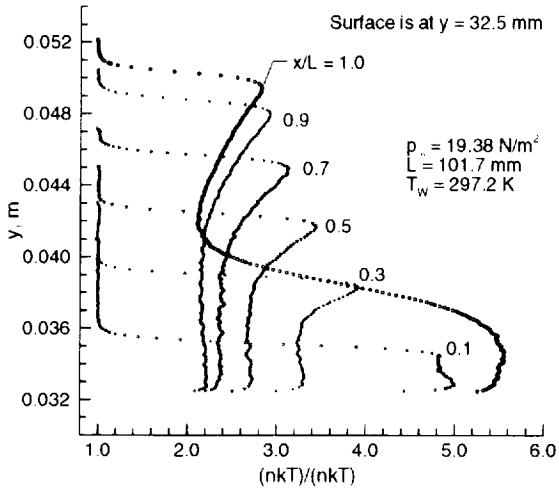

Fig. 29 Scalar pressure profiles for LENS-11 condition.

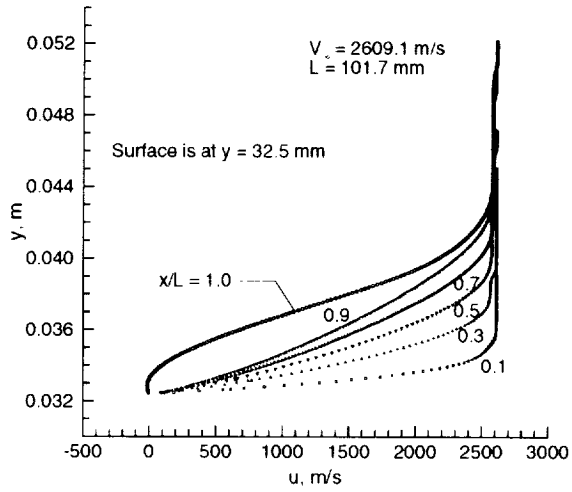

Fig. 31 Tangential velocity profiles for LENS-11 condition.

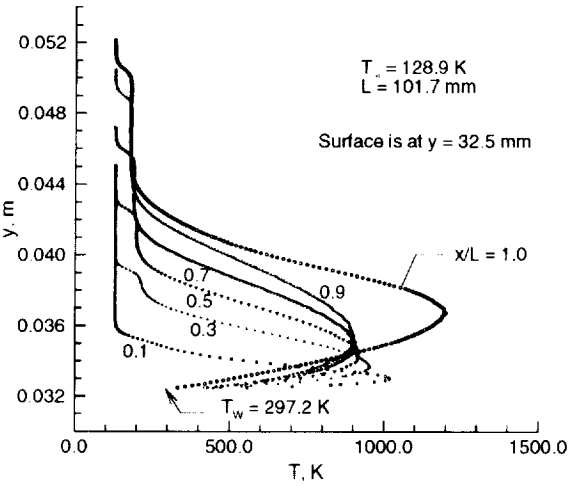

Fig. 30 Overall kinetic temperature profiles for LENS-11 condition.

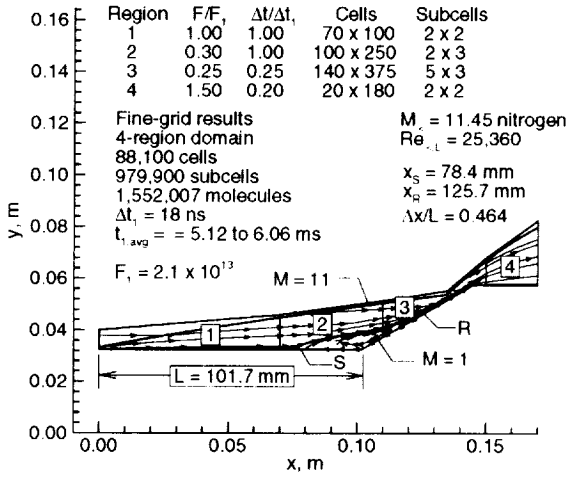

Fig. 32 Flow structure and solution parameters for LENS-19 condition.

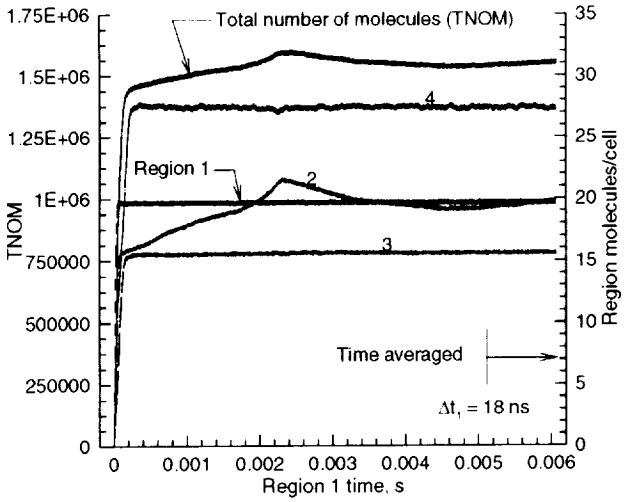

Fig. 33 Simulation history for LENS-19 condition.

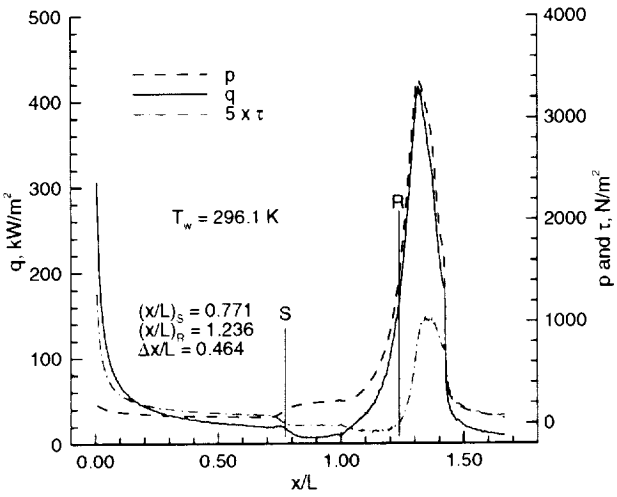

Fig. 34 Surface distributions for LENS-19 condition.

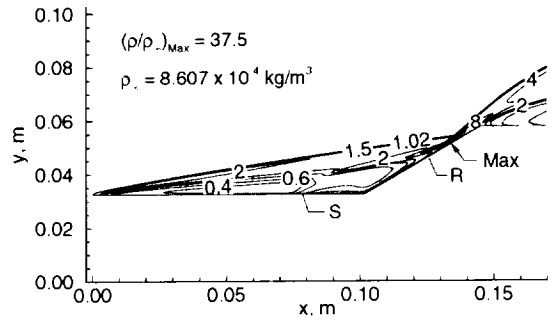

Fig. 35 Density contours for LENS-19 condition.

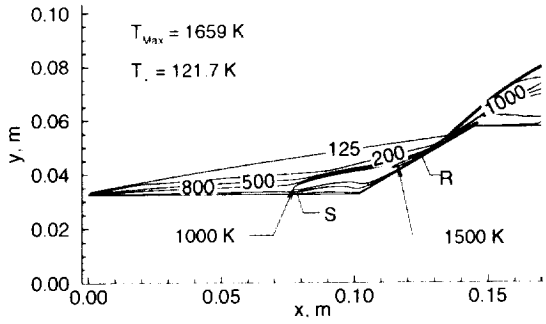

Fig. 36 Overall kinetic temperature contours for LENS-19 condition.

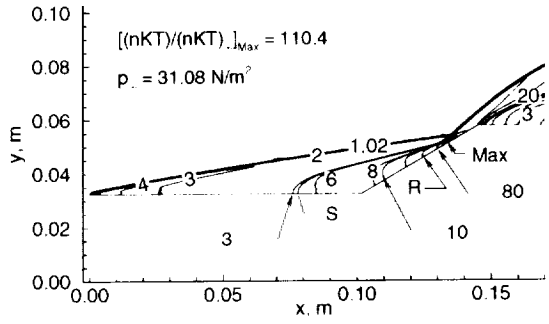

Fig. 37 Scalar pressure contours for LENS-19 condition.

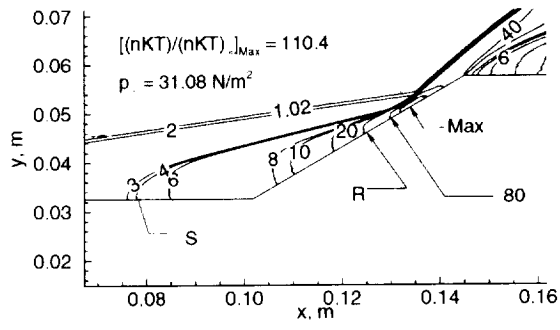

Fig. 38 Scalar pressure contours along flare for LENS-19 condition.

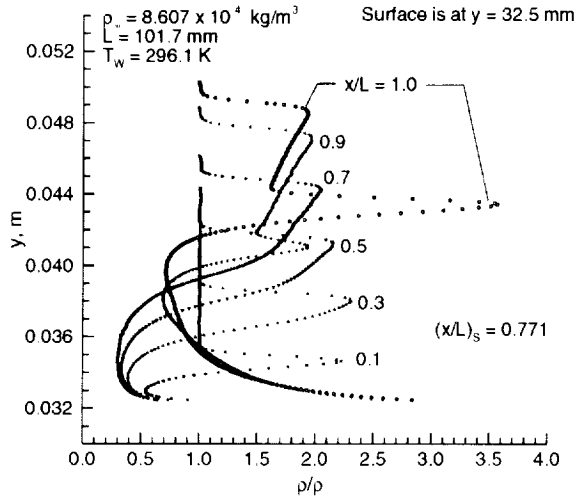

Fig. 39 Density profiles for LENS-19 condition.

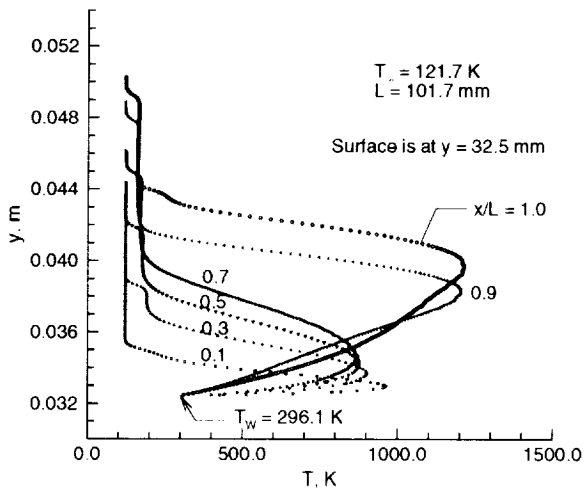

Fig. 41 Overall kinetic temperature profiles for LENS-19 condition.

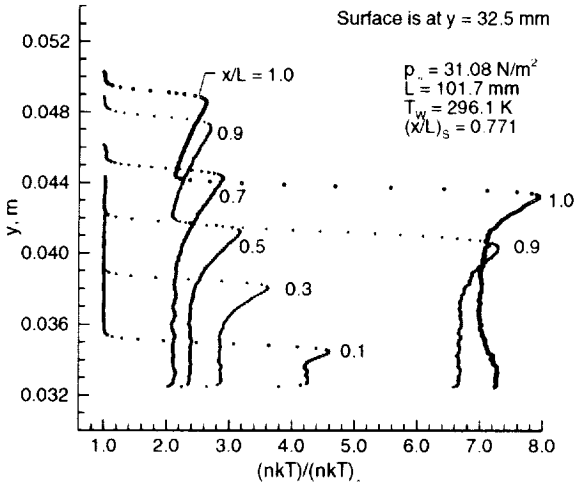

Fig. 40 Scalar pressure profiles for LENS-19 condition.

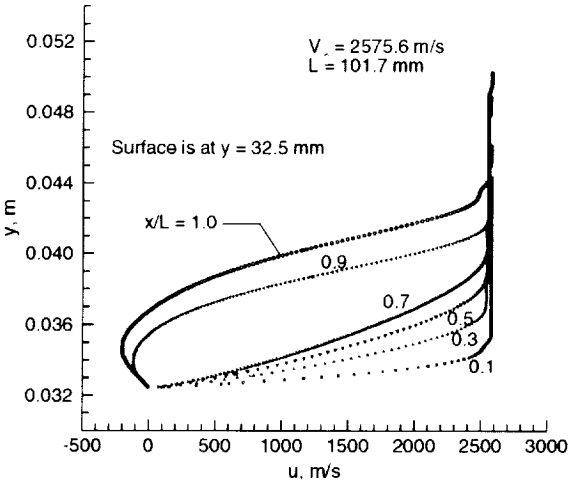

Fig. 42 Tangential velocity profiles for LENS-19 condition.

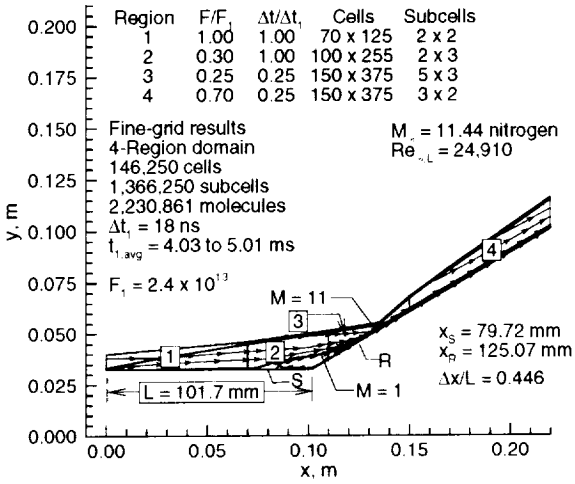

Fig. 43 Flow structure and solution parameters for LENS-9 condition.

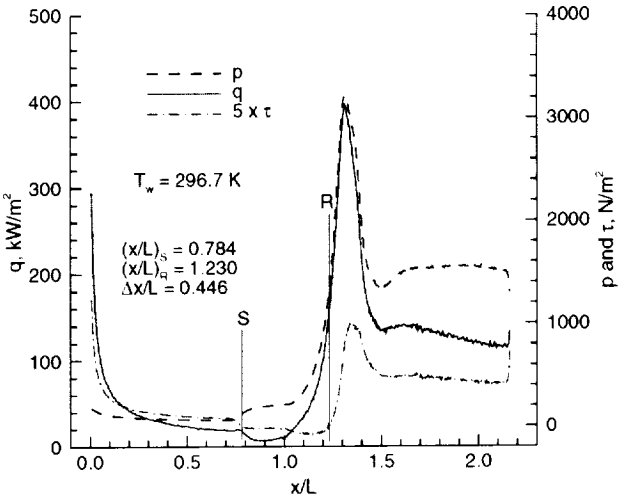

Fig. 45 Surface distributions for LENS-9 condition.

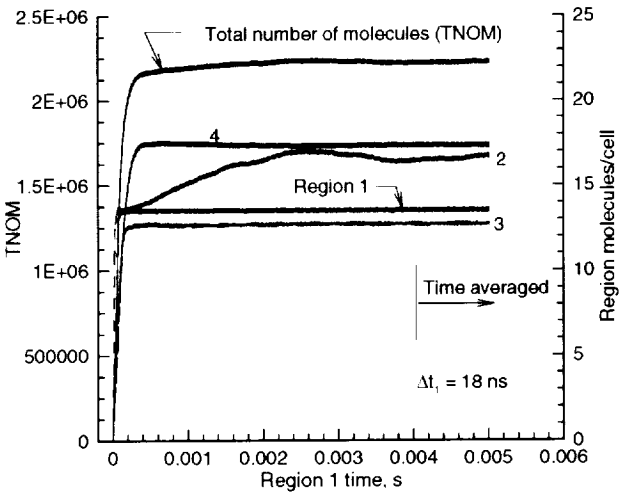

Fig. 44 Simulation history for LENS-9 condition.

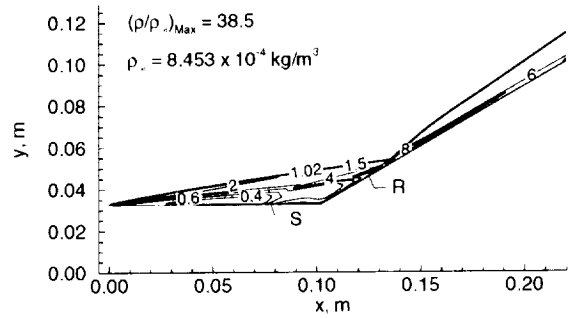

Fig. 46 Density contours for LENS-9 condition.

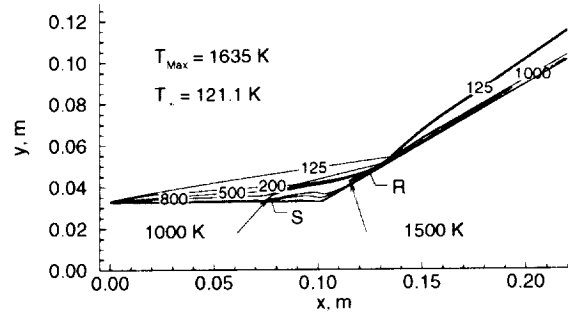

Fig. 47 Overall kinetic temperature contours for LENS-9 condition.

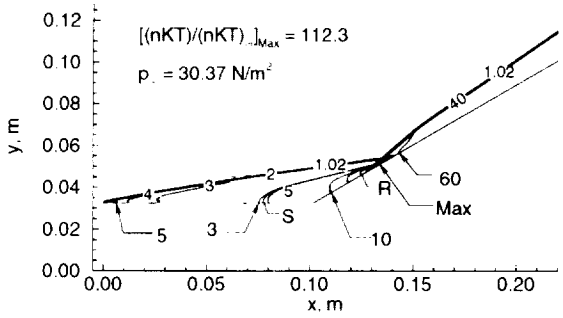

Fig. 48 Scalar pressure contours for LENS-9 condition.

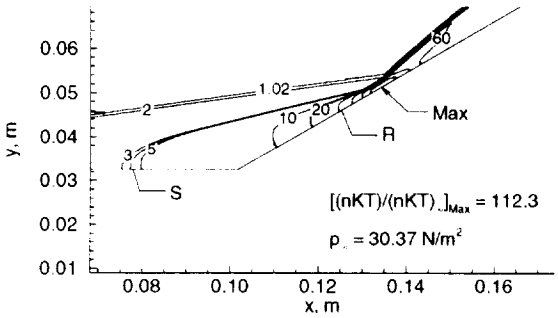

Fig. 49 Scalar pressure contours along flare for LENS-9 condition.

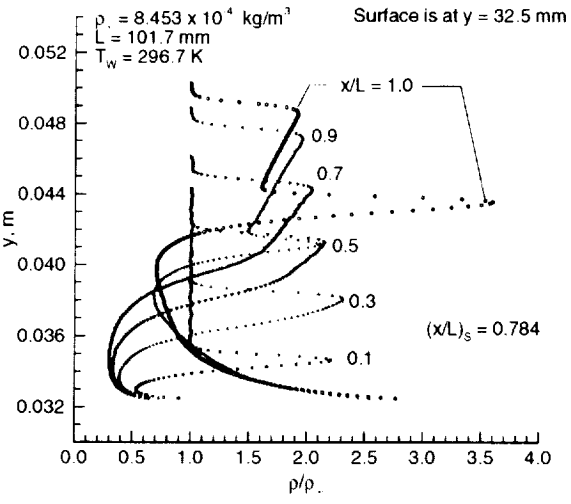

Fig. 50 Density profiles for LENS-9 condition.

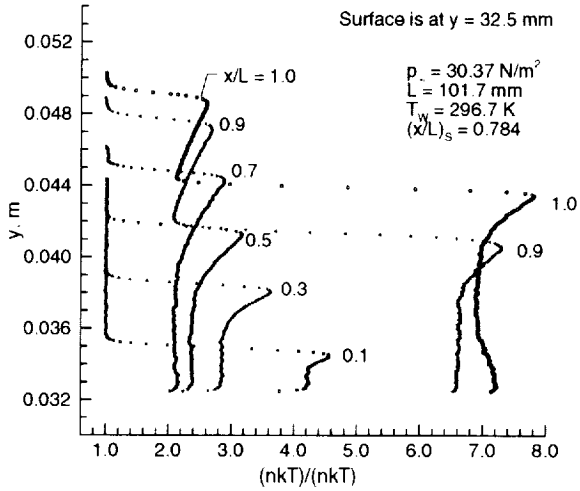

Fig. 51 Scalar pressure profiles for LENS-9 condition.

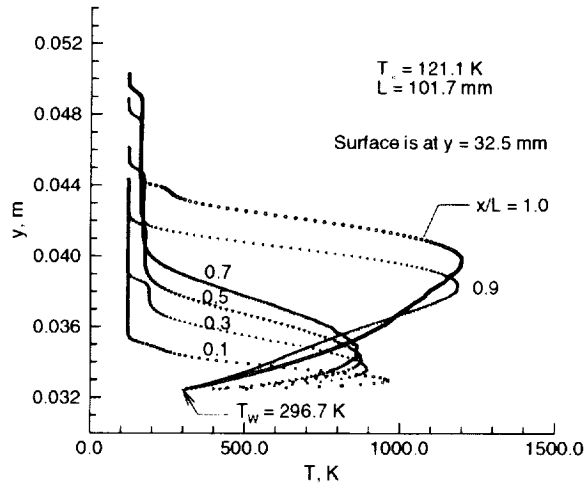

Fig. 52 Overall kinetic temperature profiles for LENS-9 condition.

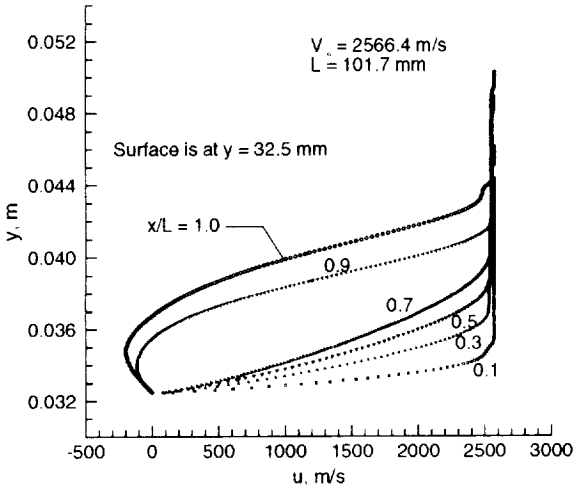

Fig. 53 Tangential velocity profiles for LENS-9 condition.

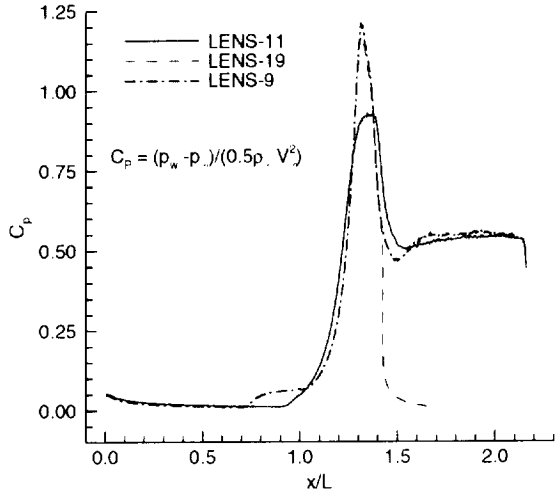

Fig. 55 Pressure coefficient results for three LENS test conditions.

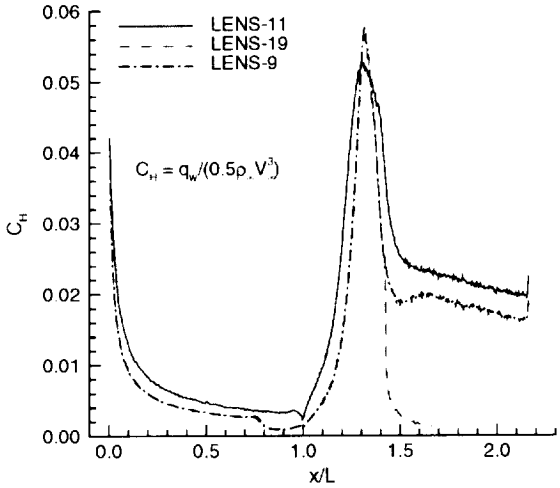

Fig. 54 Heat-transfer coefficient results for three LENS test conditions.

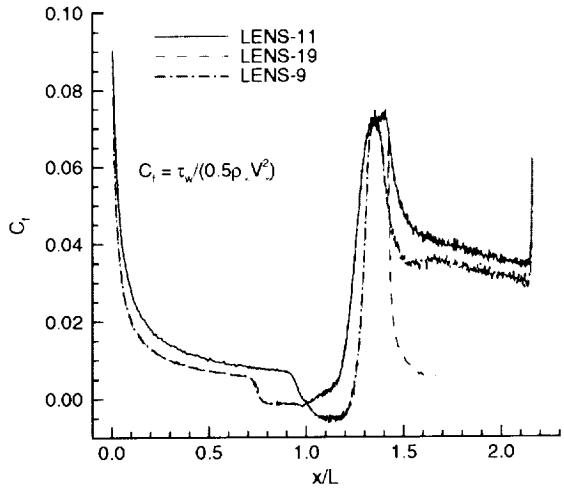

Fig. 56 Friction coefficient results for three LENS test conditions.

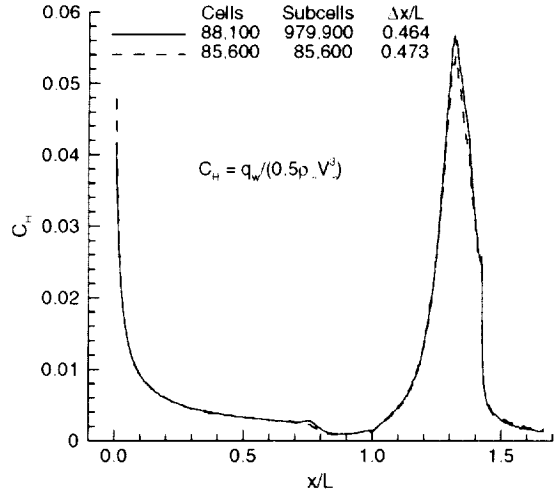

Fig. 57 Effect of grid refinement on heating rate coefficient for LENS-19 conditions.

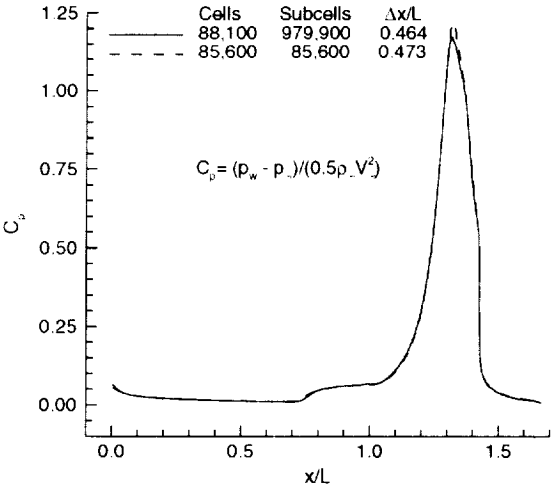

Fig. 58 Effect of grid refinement on pressure coefficient for LENS-19 conditions.

Conditions for incipient separation

Calculations have been performed to identify the conditions for incipient separation, the largest Reynolds number for which the flow remains attached, for the current hollow cylinder-flare configuration. The free-stream conditions are based on the LENS-9 test case. The Reynolds number variation is achieved by varying the free-stream density, producing the conditions identified as LENS-B through LENS-G (Table 1). Consequently, the calculations are for Mach 11.44 nitrogen at a wall temperature of 296.7 K, and the key calculations are made with the short flare. Table 2 includes information regarding the calculated locations and extent of separation, while Figs. 59 through 61 present representative surface results, primarily friction distributions.

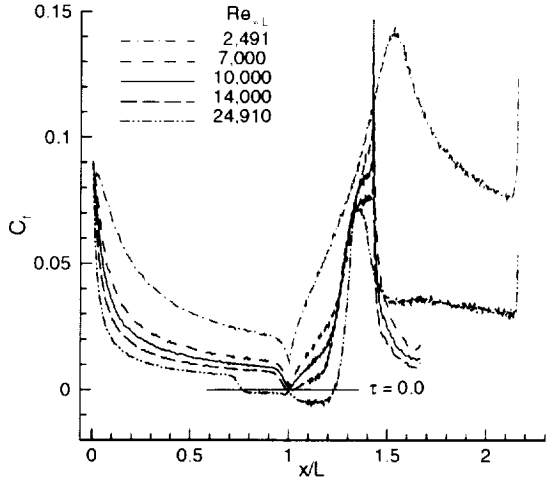

Fig. 59 Friction coefficient distributions— parametric variations (free-stream density) to identify conditions for incipient separation.

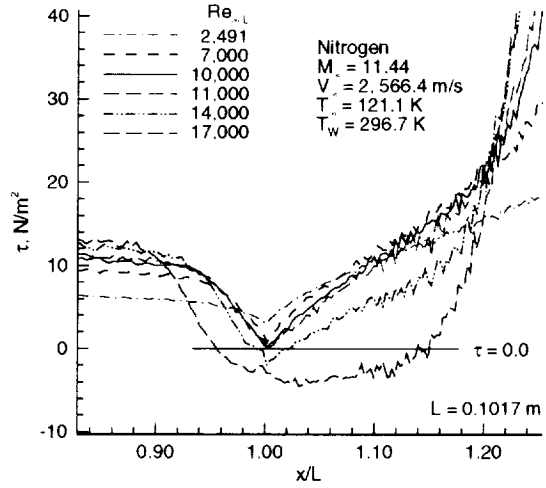

Fig. 60 Detail in separation region for various free-stream Reynolds numbers.

Based on these calculations, a free-stream Reynolds number of 10 000 is identified as the approximate condition for incipient separation. Figure 59 presents the skin friction coefficient distributions for several of the computations made for Reynolds numbers between 2 491 and 24 910. The results show the expected trend of friction coefficient decreasing with increasing Reynolds number. The data also shows that the peak value on the flare (if the long flare had been used for all calculations) moves upstream with increasing Reynolds number. Also, the shape of the distributions at the juncture of the cylinder and flare (x/L = 1) is characterized by a dimple or downward pointing depression that approaches zero for a Reynolds number of 10 000. As the Reynolds number increases

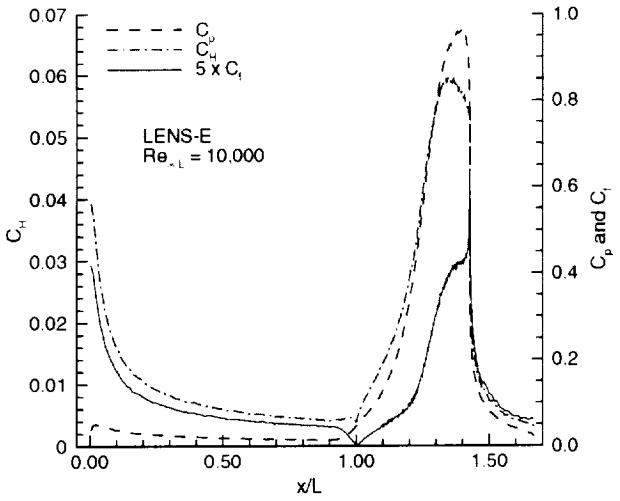

Fig. 61 Calculated surface coefficient distributions for incipient separation condition.

beyond 10 000, the direction of the dimple reverses and points in a positive direction from a negative position or value.

A more detailed view of the friction results in the separation region is presented in Fig. 60. Figure 61 presents the heating, pressure and friction coefficient distributions for the incipient separation flow conditions.

Note that the maximum surface values are not realized along the short flare for the lowest Reynolds number condition. For this flow condition, the short- and long-flare surface results are the same for all surface quantities except for the last few mm prior to the flow expansion onto the cylindrical extension. This rapid flow expansion produces a significant increase in the surface friction (not shown), as is evident in the other short-flare, higher Reynolds number results presented in Fig. 59.

Current results compared with correlations

This section discusses how the present results compare with correlations that have evolved from analyses and experimental observations.[20,24,25] The first comparison is with the incipient separation correlation based on the findings of Stollery,[25] Needham[20] and Holden[24] where the product of the free-stream Mach number and the surface deflection angle θ_i are plotted versus the hypersonic interaction parameter $\overline{\chi}$ with the experimental data supporting the following relation,

$$M_\infty \theta_i = C\sqrt{\overline{\chi}} \tag{8}$$

which can also be expressed (using Eq. 7) as

$$\theta_i = C\sqrt{\overline{\chi}} \tag{9}$$

The value of C = 80 in the previous equations has stood the test of time in successfully correlating a substantial body of both experimental data and numerical solutions. This correlation is shown as the solid line in Fig. 62. The correlation indicates that the domain at or below the solid line would be attached flow, while the domain above the incipient separation condition would experience separation.

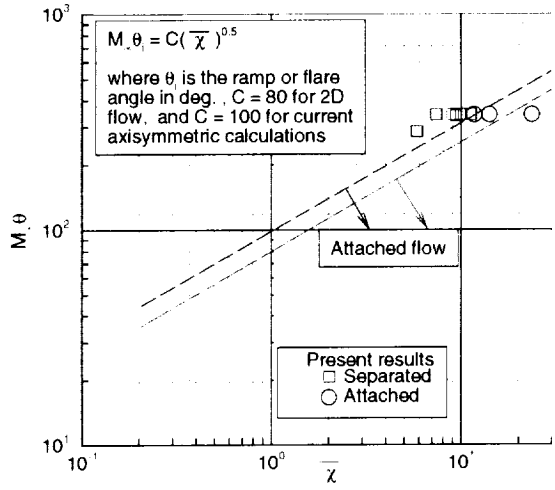

Fig. 62 Incipient separation as a function of the hypersonic viscous interaction parameter and comparison with correlation (solid line) of Ref. 20.

Also, Fig. 62 presents the current results where the circles denote results for attached flow and the squares denote separated flow. For the correlation to agree with current axisymmetric calculations, the value of the constant would have to be 100 rather than 80; that is, a higher incipient separation angle than the standard correlation. However, as has been noted by Stollery,[26] most of the experiments on which the correlation is based were done on low-aspect ratio flat plates with no side walls. A study of turbulent flows by Coleman and Stollery,[27] comparing 2D and axisymmetric tests shows an unmistakable trend in which the axisymmetric models have higher incipient separation angles. Consequently, the trend of the present findings are consistent with the trends resulting from the Coleman and Stollery[27] study. Also as pointed out by Stollery,[26] one probably would expect this trend on the physical grounds that the overall pressure rise for a given flare or flap angle is lower on the flare than on a 2D flap.

Once separation occurs, the growth of the separation region and the state of the flow (steady and laminar issues), with increasing Reynolds number, is of interest. Figures 63 and 64 present the current results for the extent of separation as a function of Reynolds and Knudsen numbers, respectively. The extent of separation increases very rapidly with Reynolds number once separation is initiated. The Mach number effect is evident with the one data point at Mach 9.57 (long flare), while all remaining values are near Mach 11.4.

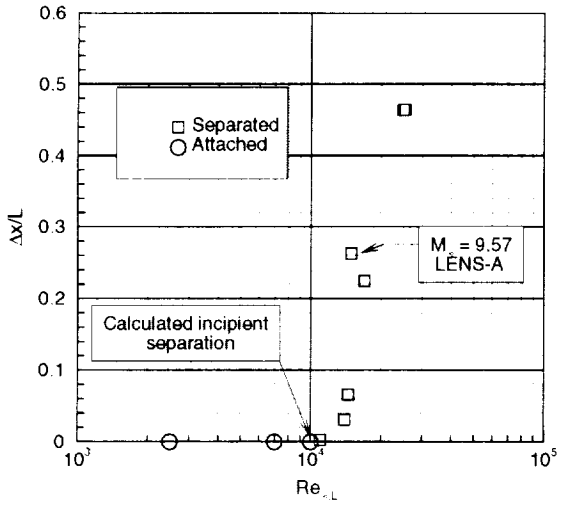

Fig. 63 Calculated extent of separation as a function of $Re_{\infty,L}$.

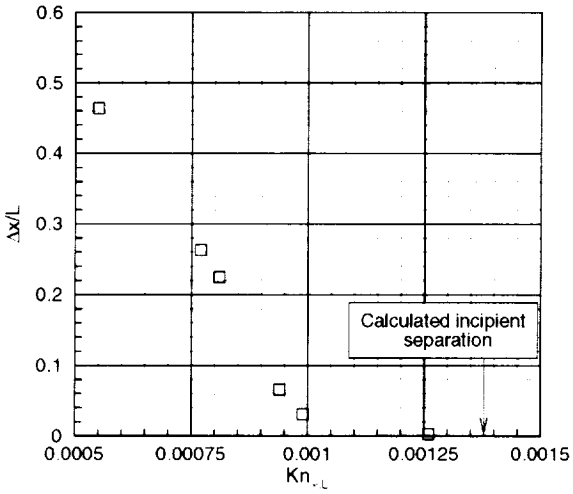

Fig. 64 Calculated extent of separation as a function of free-stream Knudsen number.

When the results are plotted as a function of Knudsen number (incorporates both Reynolds and Mach effects), the trend is as shown in Fig. 64. Once the extent of separation has achieved a relatively small value, say 3%, the separation growth is approximately linear, with decreasing Knudsen number for the range of conditions investigated.

A key issue with shock/shock and shock/boundary layer interactions is the resulting heating rate and pressure amplifications. Along the flare, the flow experiences a recompression shock and boundary layer thinning, both factors producing a peak heating that can be correlated with the peak pressure; i.e.,

$$q_{max}/q_{ref} = A(p_{max}/p_{ref})^B \qquad (10)$$

Marini[28] has presented comparisons of numerical results with a broad range of experimental measurements for sharp leading edge ramp configurations in terms of Eq. 10, where a fit is obtained for A = 0.73 and B = 0.8. The "ref" quantities are selected at a location upstream of the ramp or flare such that values are unaffected by the downstream flow deflection. The results of Marini's correlation are shown by the solid line in Fig. 65. The current results, represented by symbols (Fig. 65), agree well with the correlation. Table 3 presents detailed information concerning the current results location and magnitude of reference values, along with the maximum pressure and heating quantities along the flare.

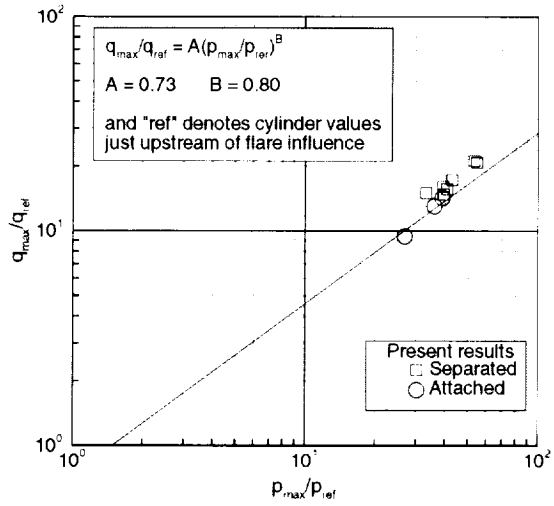

Fig. 65 Present results compared with peak heating correlation of Ref. 28 (solid line).

The current DSMC calculations for the hollow cylinder-flare configuration/s have provided results for four test conditions, one in the ONERA and three in the CUBRC test facilities. Comparisons with the ONERA data are shown to be good with the exception of surface pressure. Additional solutions are presented that examined the conditions for incipient separation. Flow-field and surface results are presented that demonstrate their sensitivity to numerical parameters and the nature of the agreement of the current results with existing correlations.

Sharp Double Cone Results

The results presented in this section are from Ref. 10, in which DSMC calculations were made for both the ONERA R5Ch and the CUBRC LENS flow conditions for model configurations that have been or will be tested. Some of these results are included to highlight situations where the shock/shock interactions are much stronger than those previously discussed for the hollow cylinder-flare cases. For the double-cone models investigated, the first cone half angle is 25°, while the second cone half angle is either 55° or 65°. The DSCM calculations for the larger half

angle cones have been made at R5Ch flow conditions for a range of model sizes and assumed variations in free-stream density. This range of flow and model parameters provided both attached and separated flows, including large separated flow regions as is described in Refs. 4 and 5. For the largest Reynolds number flow condition ($Re_{\infty,d} = 25719$) investigated in these studies, the Navier-Stokes calculations by Olejniczak[5] indicated that flow was possibly unsteady. Recent calculations by Bird[30] for this problem, using a time accurate DSMC simulation, also show the flow to be unsteady with time-varying surface pressure values in the separated region. Since experiments have not been conducted for the 25/65 double cone, only a summary of the results for the 25/55 configuration is presented.

Table 4 lists the free-stream conditions for the calculations. Table 5 presents information concerning the effect of grid resolution and flow conditions for calculated size and location of the separation region. The identifiers used for the various LENS and LENS-like flow conditions are as follows: 1) a number extension, as in LENS-28, is a CUBRC run with a run number of 28, and 2) a dual letter extension denotes a LENS-like condition where the first letter is the identifier used in Ref. 10, and the second letter "C" (cone) is used to avoid confusion with the identifiers used for the hollow cylinder-flare cases. As indicated in Table 5, calculations have not been made for an actual CUBRC test condition. The identifier code is as follows: "BC" denotes nominal pretest conditions for which grid sensitivity studies were made; "AC" denotes actual test conditions as reported in Ref. 18 (condition "A" in Table 1. of Ref. 18). Note that only minor differences exist in the flow conditions for LENS-28 and LENS-AC. "CC" denotes assumed conditions (adjustment of LENS-AC density) to achieve a specific Reynolds number.

Pretest (LENS-BC) and Test (LENS-AC) Calculations

This section focuses on results for the LENS flow conditions where the maximum model diameter d is 261.8 mm. The initial calculations were made for pretest nominal conditions (LENS-BC). A grid sensitivity study was conducted, and the results of this study, as it impacts the extent of separation ($\Delta s/L_1$ where "s" is surface distance measured from the cone vertex and L_1 is the length of the first cone) and surface heating-rate distributions, are presented in Fig. 66. The qualitative characterization of the grid listed in Fig. 66 and Table 5 is I for intermediate, C for coarse, and VC for very coarse. The finest grid used in this exercise is described as intermediate because grid independence was not demonstrated additional grid refinement is necessary to indicate whether the current intermediate grid is adequate.

Once information became available about the test

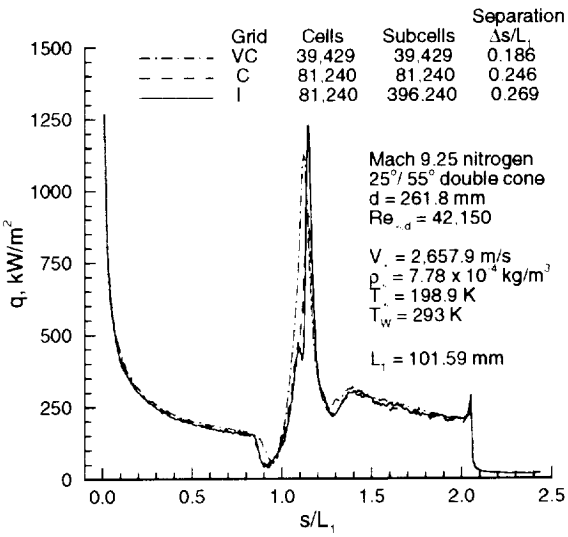

Fig. 66 Effect of grid on heating-rate results for a pretest nominal LENS flow condition.

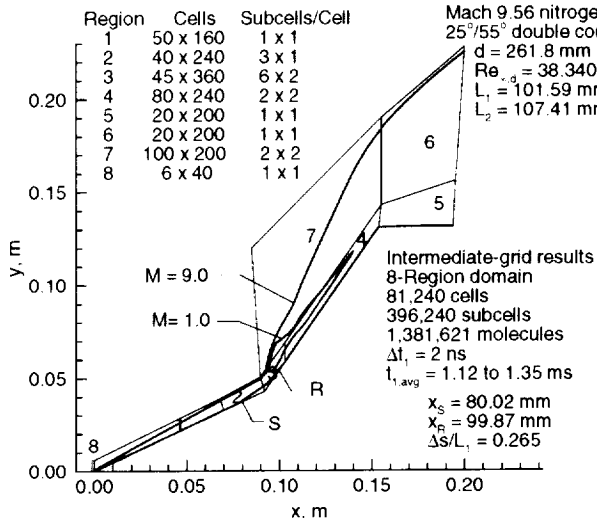

Fig. 67 Flow structure and simulation parameters for 25°/55° double cone (LENS flow).

conditions used in the CUBRC experiments,[18] the finest grid used in the pretest grid investigation was then used to make a calculation for the LENS-AC test conditions (free-stream conditions included in Fig. 68), and selected results are presented in Figs. 67 and 68. The general features of the shock layer structure are given in Fig. 67 where selected Mach contours are included, along with details of the numerical parameters used in the simulation. Values for the surface quantities are shown in Fig. 68. For the surface pressure distribution, the calculated values outside the region that are influenced by the shock/boundary layer interactions are in close agreement with the inviscid cone values (Ref. 29) of 948 N/m^2 along the 25° cone and 3710 N/m^2 along the 55° cone. Details concerning the flow structure are presented in Ref. 10 where the

Table 4 Free-stream and surface conditions for sharp double cones.

Facility	V_∞, m/s	$\rho_\infty \times 10^4$, kg/m^3	$n_\infty \times 10^{-22}$, m^{-3}	T_∞, K	p_∞, N/m^2	Gas	M_∞	T_w, K
CUBRC LENS-28	2664.0	6.545	1.407	185.6	36.05	N_2	9.59	293.3
CUBRC LENS-AC	2713.6	6.808	1.463	194.1	39.21	N_2	9.56	297.8
CUBRC LENS-BC	2657.9	7.782	1.673	198.9	45.93	N_2	9.25	293.0
CUBRC LENS-CC	2713.6	8.647	1.858	194.1	49.80	N_2	9.56	293.0
ONERA R5Ch	1418.7	4.303	0.895	51.0	6.30	Air	9.91	293.0

Table 5 Results of DSMC calculations for sharp double cones.

Cone parameters				Test		Separation	Reattachment		
Angles	L_1, mm	d, mm	Grid	condition	$Re_{\infty,d}$	x_S, mm	x_R, mm	$\Delta x/L_1$	$\Delta s/L_1$
25°/55°	101.6	261.8	I	LENS-AC	38340	80.02	99.87	0.196	0.265
25°/55°	101.6	261.8	I	LENS-BC	42150	80.01	100.10	0.198	0.269
25°/55°	101.6	261.8	C	LENS-BC	42150	80.60	99.17	0.182	0.246
25°/55°	101.6	261.8	VC	LENS-BC	42150	84.00	97.81	0.136	0.186
25°/55°	25.8	66.4	I	LENS-AC	9730	21.75	24.61	0.111	0.154
25°/55°	25.8	66.4	I	LENS-CC	12360	21.45	24.74	0.127	0.179
25°/55°	25.8	66.4	I	R5Ch	12360	21.17	25.36	0.162	0.229

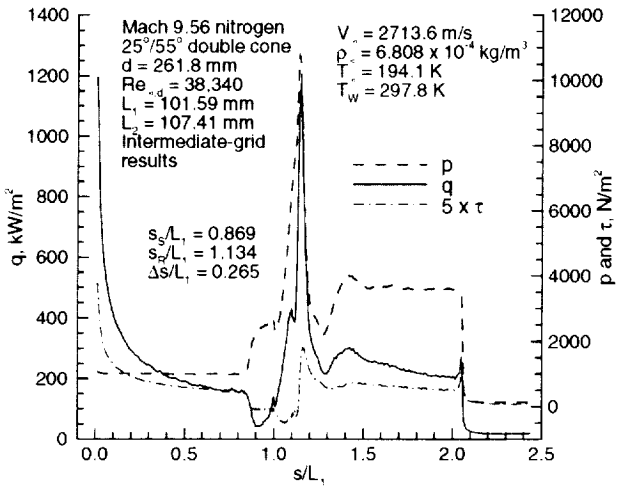

Fig. 68 Calculated surface results for double-cone model at a LENS test condition.

calculations show that the maximum values for density and scalar pressure are 155 and 319 times their respective free-stream values and that there is a maximum overall kinetic temperature of 3104 K. Comparisons of translational and internal temperature profiles show that the thermal nonequilibrium effects are confined primarily to the outer bow shock crossings. Opportunities will exist for comparing the present results with the experimental measurements (heating-rate and pressure distributions) when the CUBRC data are released.[9]

25°/55° Cone With A Diameter of 66.45 mm—LENS and R5Ch Conditions

To examine the effect of different experimental test conditions on surface and flow-field features, a common model (one that could be potentially tested in R5Ch) is used for making calculations at both ONERA R5Ch and LENS nominal test conditions. The model configuration is one that has been used in the CUBRC tests, but the maximum model diameter is 66.45 mm rather than the 261.8-mm-diameter model tested. Reference 10 presents information concerning flow-field features and computational parameters for the smaller models. Figures 69 through 71 include information concerning surface results for heating, pressure, and friction coefficients, respectively. Table 5 provides information concerning the location and extent of separation.

When the calculation is made for the LENS-AC test conditions, the size or extent of the shock layer is slightly smaller, and the size of the subsonic region and extent of separation are noticeably reduced when compared with the results for the R5Ch flow conditions (see Ref. 10). Data are also included for a flow condition referred to as LENS-CC, where an adjustment to the density of the LENS-AC test condition is made to produce a larger free-stream Reynolds number, a value equal to that of the R5Ch test condition. The surface heating, pressure, and friction coefficient results presented in Figs. 69 through 71 show to what extent the distributions are consistent. For the surface region where separation occurs, the surface coefficient values are much larger for the LENS test conditions

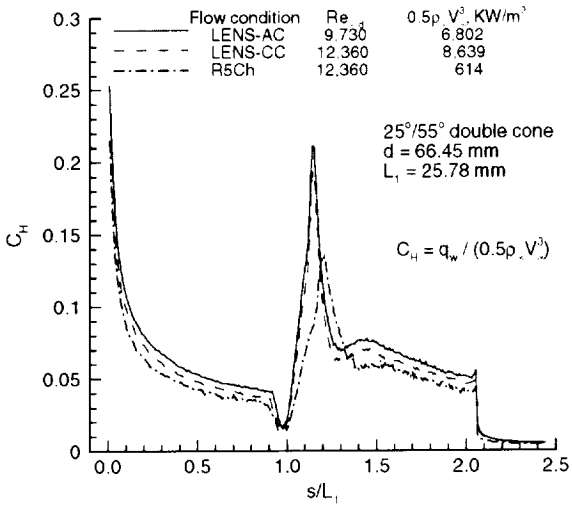

Fig. 69 Heat-transfer coefficient distributions for double-cone models.

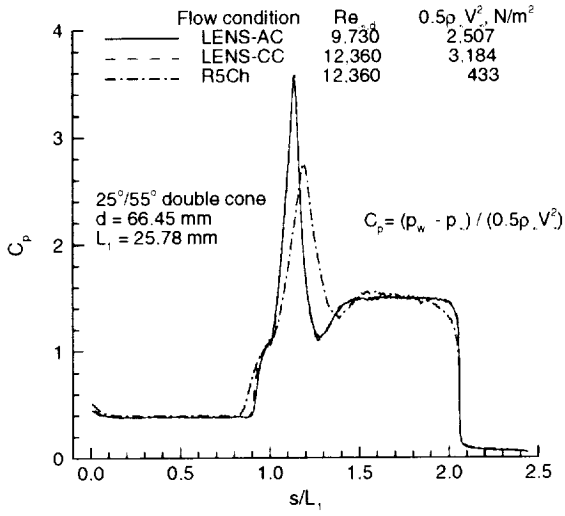

Fig. 70 Pressure coefficient distributions for double-cone models.

than those for the R5Ch condition. Of course, the dimensional heating and pressure values are much larger for the LENS conditions, about an order of magnitude difference in heating rates. The effect of increasing the free-stream density of the LENS-AC condition to produce the LENS-CC conditions (same Reynolds number as the R5Ch case) is clearly evident in the heating and friction coefficient distributions and extent of separation (Table 5), but has a minor effect on the pressure coefficient distribution.

Concluding Remarks

Results of a computational study are presented for Mach 9.3 to 11.4 flow about hollow cylinder flare and sharp double cone models where the combination of model configurations, size, and flow conditions produce a significant range of shock/shock and shock/boundary layer interactions. The computations are made with the direct simulation Monte Carlo (DSMC) method, hence, low Reynolds number flows. The results presented provide insight into the nature of the shock interactions, their impact on surface quantities, and the sensitivity of the results to computational parameters for flow conditions that can be produced in current ground-based facilities.

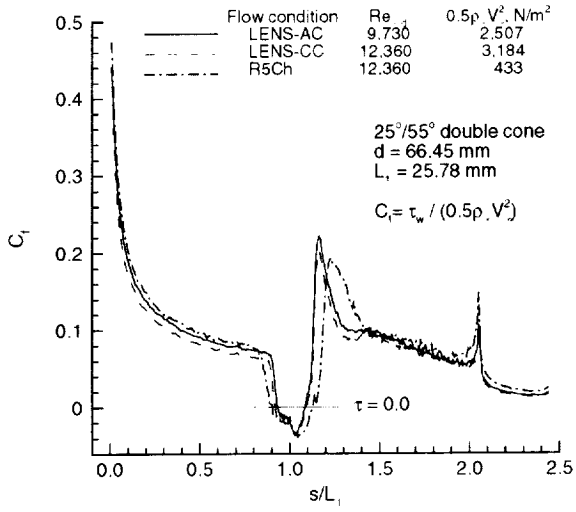

Fig. 71 Friction coefficient distributions for double-cone models.

Results of the hollow cylinder-flare calculations are compared with the experimental surface measurements made in the ONERA R5Ch wind tunnel (Mach 9.91 air at a $Re_{\infty,L} = 18916$). The extent of the calculated separation region is very sensitive to the grid resolution used a coarse grid results in a smaller separation region. Results for the finest grid investigated show very good agreement with the experimental measurements for the separation and reattachment locations and surface heating. For surface pressure, the agreement between calculation and measurement is poor the calculated values are uniformly high along both the cylinder and flare by a factor of 1.4. Additional DSMC calculations are made for the cylinder to examine the impact of additional refinement of solution parameters and leading edge treatment, and the results show no significant impact on the previously reported results. Based on these findings, it is believed the DSMC results for surface pressure are correct along the cylinder and should be reasonably accurate for the flare.

Also, DSMC results are presented for two hollow cylinder-flare models, one having the same outer surface as the ONERA model and one with a longer flare, which has been tested for a range of conditions in the CUBRC LENS tunnel. Calculations are made for three of the LENS test conditions for nominal Mach

11.4 nitrogen flow at $Re_{\infty,L}$ of 14 490 to 25 360). Additional calculations were made at lower Reynolds number values (assumed density variations) to calculate the conditions for incipient separation. Information concerning the effect of grid resolution is presented, along with detailed data concerning surface results and flow structure. Comparisons of the calculated data with existing correlations based on experimental measurements are consistent with respect to the following: 1) qualitative trends as to the effect of Mach number and Reynolds number on the extent of separation and upstream influence of a compression flare (ramp); 2) qualitative and quantitative agreement of peak heating and pressure along flare; and 3) the conditions for incipient separation.

For the 25°/55° double-cone configuration models, the extent of separation, as a function of flow conditions, is demonstrated for both LENS and R5Ch flow conditions. Results of a grid sensitivity investigation are discussed, and surface results are presented for flow conditions (Mach 9.56 nitrogen at a $Re_{\infty,L} = 38\,340$) that are approximately the same as those of a LENS-28 test that has been completed.

Opportunities will exist for comparing some of the current results for both the hollow cylinder-flare and double cone configurations with experimental measurements for surface heating and pressure distributions.

ACKNOWLEDGMENTS

The author wishes to acknowledge the assistance of B. Chanetz and T. Pot of ONERA, Chalais-Meudon, for providing information regarding their experiments and the results of their measurements. Also, the author wishes to acknowledge the assistance of Michael Holden of CUBRC for providing information regarding the model configurations and flow conditions used in the LENS tests.

References

[1]Bird, G. A.; *Molecular Gas Dynamics and the Direct Simulation of Gas Flows*. Oxford: Clarendon Press, 1994.

[2]Moss, J. N., Dogra, V. K., and Price, J. M.; DSMC Simulations for a Hollow Cylinder-Flare Configuration. AIAA Paper 94-2015, June 1994.

[3]Moss, J. N., Dogra, V. K., Price, J. M., and Hash, D. B.; Comparison of DSMC and Experimental Results for Hypersonic External Flows. AIAA Paper 95-2028, June 1995.

[4]Moss, J. N., and Olejniczak, J.; Shock-Wave/Boundary-Layer Interactions in Hypersonic Low Density Flows. AIAA Paper 98-2668, 1998.

[5]Moss, J. N., Olejniczak, J., Chanetz, B., and Pot, T.; Hypersonic Separated Flows at Low Reynolds Number Conditions. *Proceedings of the 21st International Symposium on Rarefied Gas Dynamics*. Brun, Campargue, Gatignol, and Lengrand, eds., Cepadues-Editions, Toulouse, France, Vol. II, 1999, pp. 617-624.

[6]Chanetz, B., Benay, R., Bousquet, J.-M., Bur, R., Pot, T., Grasso, F. and Moss, J.; Experimental and Numerical Study of the Laminar Separation in Hypersonic Flow. *Aerospace Science and Technology*, No. 3, 1998, pp. 205-218.

[7]Chanetz, B., Bur, R., Pot, T., Pigache, D., Grasso, F., and Moss, J.; Experimental and Numerical Study of the Laminar Separation in Hypersonic Flow. Paper presented at ECCOMAS 2000, Barcelona, Spain, Sept. 11-14, 2000.

[8]Moss, J. N.; *DSMC Simulation of Separated Flows about Flared Bodies at Hypersonic Conditions*. presented at the ECCOMAS 2000, Barcelona, Spain, Sept. 11-14, 2000. Available as NASA TM-2000-210539, October 2000.

[9]Holden, M. and Harvey, J.; Experimental Measurements over Cone/Cone and Cylinder Flare Configurations in Laminar Hypervelocity Flows. AIAA Paper 2001-1031, Jan. 2001.

[10]Moss, J. N.; *DSMC Simulations of Shock Interactions About Sharp Double Cones*. presented at the 22nd International Symposium on Rarefied Gas Dynamics, Sydney, Australia, July 9-14, 2000. Available as NASA TM-2000-210318, August 2000.

[11]Anderson, J. D., Jr.; *Hypersonic and High Temperature Gas Dynamics*. McGraw-Hill Book Co., New York, 1989.

[12]Moss, J. N., and Chun, Ch.-H.; Hypersonic Rarefied Flow about A Compression Corner–DSMC Simulation and Experiment. AIAA Paper 91-1313, 1991.

[13]Bird, G. A.; The G2/A3 Program System Users Manual, Version 1.8, March 1992.

[14]Borgnakke, C. and Larsen, P. S.; Statistical Collision Model for Monte Carlo Simulation of Polyatomic Gas Mixture. *Journal of Computational Physics*, Vol. 18, No. 4, 1975, pp. 405-420.

[15]*Hypersonic Experimental and Computational Capability, Improvement and Validation*. AGARD AR 319, edited by J. Muylaert, A. Kumar, and C Dujarric, Vol. II, Dec. 1998.

[16]Grasso, F. and Marini, M.; Synthesis of T2-97 Hollow Cylinder Flare Problem. *Proc. of the First Europe-US High Speed Flow Field Database Workshop*, AIAA, 1998, pp 202-207.

[17]Candler, G. V., Nompelis, I., and Holden, M. S.; Computational Analysis of Hypersonic Laminar Viscous-Inviscid Interactions. AIAA Paper 2000-0532, Jan. 2000.

[18]Holden, M.; Experimental Studies of Laminar Separated Flows Induced by Shock Wave/Boundary Layer and Shock/Shock Interaction in Hypersonic Flows for CFD Validation. AIAA Paper 2000-0930, Jan. 2000.

[19]Chanetz, B.; *Study of Axisymmetric Shock Wave/Boundary Layer Interaction in Hypersonic Laminar Flow*. ONERA Technical Report TR No. 42/1623, Feb. 1995.

[20]Needham, D., and Stollery, J.; Boundary Layer Separation in Hypersonic Flow. AIAA Paper 66-455, 1966.

[21]Markelov, G. N., Kudryavtsev, A. N., and Ivanov, M. S.; Continuum and Kinetic Simulation of Laminar Separated Flow at Hypersonic Speeds. *Journal of Spacecraft and Rockets*, Vol. 37, No. 4, July-August 2000, pp. 499-506.

[22]Holden, M. S.; Two-dimensional Shock Wave-Boundary Layer Interactions in High Speed Flows. Part II, *Experimental Studies on Shock Wave-Boundary Layer Interactions*, AGAR Dograph AG-203, 1975, pp 41-110.

[23]Delery, J. M.; *Shock Interference Phenomena in Hypersonic Flows*. The Third Joint Europe/US Short Course in Hypersonics, University of Aachen, Germany, 1990.

[24]Holden, M. S.; *A Review of the Characteristics of Regions of Shock Wave/Boundary Layer Interaction*. AGARD Rept. 764, 1989.

[25]Stollery, J. L.; *Laminar and Turbulent Boundary Layer Separation at Supersonic and Hypersonic Speeds*. AGARD CP-168, "Flow Separation," 1966

[26]Stollery, J. L.; private communication, Nov. 2000.

[27]Coleman, G. T., and Stollery, J. L.; Incipient Separation of Symmetric Hypersonic Turbulent Boundary Layers. *AIAA Journal*, Vol. 12, No. 1, pp 119-120, 1974.

[28]Marini, M.; *A Review of Shock-Wave Boundary-Layer Laminar Interactions on Sharp Leading Edge Ramp Configurations*. presented at the ECCOMAS 2000, Barcelona, Spain, Sept. 11-14, 2000.

[29]Ames Research Staff; *Equations, Tables, and Charts for Compressible Flow.* NACA Report 1135, 1953.
[30]Bird, G. A.; private communication, Aug. 2000.